The Astrophysical Journal, 926:219 (17pp), 2022 February 20 https://doi.org/10.3847/1538-4357/ac3763


# Dramatic Changes in the Observed Velocity of the Accretion Disk Wind in MCG-03-58-007 Are Revealed by XMM-Newton and NuSTAR

V. Braito[1,2], J. N. Reeves[1,2], G. Matzeu[3], P. Severgnini[4], L. Ballo[5], C. Cicone[6], R. Della Ceca[4], M. Giustini[7], and M. Sirressi[8]

[1] INAF, Osservatorio Astronomico di Brera Via Bianchi 46 I-23807 Merate (LC), Italy
[2] Department of Physics, Institute for Astrophysics and Computational Sciences, The Catholic University of America, Washington, DC 20064, USA
[3] Department of Physics and Astronomy—DIFA, University of Bologna, Via Gobetti 93/2, I-40129 Bologna, Italy
[4] INAF—Osservatorio Astronomico di Brera, Via Brera 28, I-20121 Milano, Italy
[5] European Space Astronomy Centre (ESA/ESAC), E-28691 Villanueva de la Canada, Madrid, Spain
[6] Institute of Theoretical Astrophysics, University of Oslo, P.O. Box 1029 Blindern, 0315 Oslo, Norway
[7] Centro de Astrobiología (CSIC-INTA), Camino Bajo del Castillo s/n, Villanueva de la Cañada, E-28692 Madrid, Spain
[8] Department of Astronomy, AlbaNova University Center, Stockholm University, SE-10691 Stockholm, Sweden
*Received 2021 August 2; revised 2021 October 14; accepted 2021 November 5; published 2022 February 25*

## Abstract

Past X-ray observations of the nearby Seyfert 2 MCG-03-58-007 revealed the presence of a powerful and highly variable disk wind, where two possible phases outflowing with $v_{\rm out1}/c \sim -0.07$ and $v_{\rm out2}/c \sim -0.2$ were observed. Multi-epoch X-ray observations, covering the period from 2010 to 2018, showed that the lower-velocity component is persistent, as it was detected in all the observations, while the faster phase outflowing with $v_{\rm out2}/c \sim -0.2$ appeared to be more sporadic. Here we present the analysis of a new monitoring campaign of MCG-03-58-007 performed in 2019 May–June and consisting of four simultaneous XMM-Newton and NuSTAR observations. We confirm that the disk wind in MCG-03-58-007 is persistent, as it is detected in all the observations, and powerful, having a kinetic power that ranges between 0.5% and 10% of the Eddington luminosity. The highly ionized wind ($\log(\xi/{\rm erg\,cm\,s^{-1}}) \sim 5$) is variable in both the opacity and, remarkably in its velocity. This is the first time where we have observed a substantial variability of the outflowing velocity in a disk wind, which dropped from $v_{\rm out}/c \sim -0.2$ (as measured in the first three observations) to $v_{\rm out}/c \sim -0.074$ in just 16 days. We conclude that such a dramatic and fast variability of the outflowing velocity could be due to the acceleration of the wind, as recently proposed by Mizumoto et al. Here, the faster wind, seen in the first three observations, is already accelerated to $v_{\rm out}/c \sim -0.2$, while in the last observation our line of sight intercepts only the slower, pre-accelerated streamline.

*Unified Astronomy Thesaurus concepts:* Active galaxies (17); High energy astrophysics (739); X-ray active galactic nuclei (2035)

## 1. Introduction

It is now widely recognized that high-velocity outflows are an almost ubiquitous and important phenomenon of the central regions of active galactic nuclei (AGN; Tombesi et al. 2010, 2012; Gofford et al. 2013, 2015). They were initially discovered through observations of blueshifted absorption features from iron K-shell transitions in the X-ray spectra of bright AGN (PDS 456, Reeves et al. 2003; PG1211+143, Pounds et al. 2003; APM 08279+5255, Chartas et al. 2002). The inferred high velocities, reaching up to $\sim$0.3 $c$, and high-ionization state immediately suggested that they originate from within a few hundred gravitational radii from the central black hole (King & Pounds 2015). These winds are also massive, and the inferred outflow rates can approach up to a few $M_{\odot}$ yr$^{-1}$, matching the typical accretion rates of AGN. This indicates that they are probably linked to the accretion process itself (King 2003, 2010; King & Pounds 2015) and driven either by the radiation pressure (Proga et al. 2000; Proga & Kallman 2004; Sim et al. 2008, 2010b), by magneto-rotational forces (MHD models; Kato et al. 2004; Kazanas et al. 2012; Fukumura et al. 2010, 2017) or a combination of both.

Although they can be affected by high uncertainties, the corresponding kinetic powers are typically of the order of a few percent of the bolometric luminosity of the AGN and thus matching or exceeding the conventional threshold of $L_{\rm KIN}/L_{\rm bol} \sim 0.5\%$–$5\%$ for efficient AGN feedback on the host galaxy (Hopkins & Elvis 2010; Di Matteo et al. 2005). These ultra-fast outflows may thus play an important role in shaping the observed AGN–host galaxy relationships, like the $M$–$\sigma$ relation (Magorrian et al. 1998; Ferrarese & Merritt 2000; Gebhardt et al. 2000). Potentially, they can simultaneously self regulate the growth of the supermassive black hole (SMBH; King & Pounds 2015; Zubovas & King 2012, 2016) and drive the massive, kiloparsec-scale molecular outflows (Cicone et al. 2014, 2015; Fiore et al. 2017; Fluetsch et al. 2019; Lutz et al. 2020), which can sweep away the interstellar medium (ISM) and quench the star formation.

Nonetheless, the real connection between the small-scale disk winds, detected in the X-ray spectra, and the large-scale molecular outflows is not proven yet, as there are still too few examples of powerful disk wind with deep Atacama Large Millimeter/submillimeter Array (ALMA) observations and vice versa. In this respect, the first detections of powerful X-ray disk winds in two ultraluminous infrared galaxies with massive large-scale molecular outflows (Mrk 231, Feruglio et al. 2015;

IRASF 11119+3257, Tombesi et al. 2015) appeared to follow the prediction for the so-called blast-wave scenario (King 2010; Faucher-Giguère & Quataert 2012). According to this model, when the nuclear disk wind propagates and interacts with the ISM, it produces a shocked wind, which sweeps up the ambient gas. In particular, if the Compton cooling of the shock is not efficient, in the so-called "energy-driven" case, the large-scale outflow will receive a momentum boost. However, recent results on other ultra-fast disk winds observed with ALMA show that not all outflows lie on the energy-conserving relation. In the majority of the cases, the momentum rate of the large-scale outflows is well below the prediction from the energy-conserving scenario and more in line with a momentum-conserving wind (see Veilleux et al. 2020 and references therein). We note that for the prototype of the fast disk winds PDS 456 (Bischetti et al. 2019), the powerful wind of I Zw 1 (Reeves & Braito 2019) as well as for the powerful disk wind at the core of this work (Sirressi et al. 2019), an energy-conserving wind can be clearly ruled out. This does not imply that the disk winds do not impact the star formation in the host galaxy, but rather that they do not always couple efficiently with the ISM (Mizumoto et al. 2019; Veilleux et al. 2020).

Generally, when we have an estimate of the energetics of both the small- and large-scale phases of the outflow, they are affected by large uncertainties, which further complicates the interpretation of the results. In the X-ray band, we can improve our accuracy on the estimates of the energetics by applying self-consistent disk-wind models. Recently, various groups have been developing new models for radiatively driven (Sim et al. 2008, 2010a, 2010b; Hagino et al. 2015, 2016; Nomura & Ohsuga 2017; Nomura et al. 2020; Mizumoto et al. 2021) as well as MHD winds (Fukumura et al. 2010, 2015; Kazanas et al. 2012). These models can now be applied to the X-ray spectra of AGN winds (e.g., Reeves & Braito 2019; Luminari et al. 2018) to derive more robust estimates of the mass outflow rates, the terminal velocities, and hence the wind energetics.

Another important aspect that needs to be considered is that disk winds are generally extremely variable on timescales that can be as short as a few weeks or even days (e.g., PDS 456; Matzeu et al. 2016; Reeves et al. 2018a), whereby they can vary in ionization, column density ($N_{\rm H}$), and also velocity (e.g., PDS 456, Reeves et al. 2018a; Matzeu et al. 2017; IRASF 11119+3257, Tombesi et al. 2017; PG 1211+143, Reeves et al. 2018b; APM 08279+5255, Saez & Chartas 2011; IRAS 13224-3809, Parker et al. 2018; MCG-03-58-007, Braito et al. 2018; Matzeu et al. 2019, hereafter B18 and M19). Fast variability of the properties of the disk winds is not unexpected, as disk-wind simulations predict that the stream is not a homogeneous and constant flow (Proga & Kallman 2004; Giustini & Proga 2012; Dannen et al. 2020; Waters et al. 2021). Depending on the observation, our line of sight could thus intercept different clumps or streams of the winds or we could be witnessing a reaction of the wind to the changes in the luminosity of the X-ray source. A direct correlation between the outflowing velocity and the luminosity of the ionizing continuum has been reported for PDS 456 (Matzeu et al. 2017), IRAS 13224–3809 (Chartas & Canas 2018), and APM 08279 +5255 (Saez & Chartas 2011), while a correlation between the ionization of the disk wind and the X-ray luminosity was also reported for IRAS 13224–3809 by Pinto et al. (2018). These results suggest that the incident radiation plays an important role in driving the disk winds and when the luminosity and radiation pressure increase, a faster and/or more ionized wind is driven.

Here, we present the results of a monitoring campaign of MCG-03-58-007, consisting of four simultaneous XMM-Newton and Nuclear Spectroscopic Telescope Array (NuSTAR) observations taken in 2019 May–June. MCG-03-58-007 is a bright and nearby Seyfert 2 galaxy ($F_{2-10\rm keV} \sim 2$–$4 \times 10^{-12}$ erg cm$^{-2}$ s$^{-1}$, $z = 0.03233$; Sirressi et al. 2019), which hosts one of the most powerful and extremely variable ultra-fast disk winds. MCG-03-58-007 is currently optically classified as a Seyfert 2, but the host galaxy appears to be viewed at 37 deg (Sirressi et al. 2019). Therefore unless there is a clear misalignment between the central accretion disk and the host galaxy, our line of sight could intercept the nuclear accretion disk wind only grazing the outer edge of the putative torus, which could also coincide with the outer and colder part of the wind. MCG-03-58-007 is also another clear case where the large-scale outflow, detected in the central ∼4 kpc, has not received a strong momentum boost. The CO(1-0) emission line seen in the ALMA observation traces a low-velocity ($v_{\rm CO} \sim 170$ km s$^{-1}$) molecular outflow, whose kinetic power is at least two orders of magnitude below the expected value for an energy-conserving wind ($\dot{E}_{\rm Mol}/\dot{E}_{\rm X} \sim 4 \times 10^{-3}$; Sirressi et al.2019).

### 1.1. Previous X-Ray Observations of MCG-03-58-007

The disk wind of MCG-03-58-007 was first discovered thanks to a deep Suzaku (Mitsuda et al. 2007) observation performed in 2010, where two deep ($EW \sim 300$ eV) blueshifted absorption troughs at $E = 7.4 \pm 0.1$ keV and $E = 8.5 \pm 0.2$ keV (B18) were detected. These features were associated with two zones of a highly ionized (log ($\xi$/ erg cm s$^{-1}$) ∼ 5.5) and high column density ($N_{\rm H} \sim 5 - 8 \times 10^{23}$ cm$^{-2}$) wind outflowing with $v_{\rm out1}/c \sim -0.1$ and $v_{\rm out2}/c \sim -0.2$. The presence of a persistent fast disk wind was subsequently confirmed by follow-up observations performed in 2015 simultaneously with XMM-Newton and NuSTAR, in 2016 with Chandra, and in 2018 with Swift. The first follow-up confirmed the presence of the slow component of the wind, but not the ∼8.5 keV feature, and it revealed a remarkable variability of the disk wind, where we witnessed an X-ray eclipse that lasted $\Delta t \sim 120$ ks. This occultation was ascribed to a higher-opacity streamline of the wind, outflowing at $v_{\rm out} \sim -0.124\,c$, which crossed our line of sight (B18). Indeed, the observed spectral change could not be accounted for by variations of the $N_{\rm H}$ of the neutral absorber (M19). Chandra (in 2016) and Swift (in 2018) caught MCG-03-58-007 in a relatively brighter state ($F_{2-10keV} \sim 4 \times 10^{-12}$ erg cm$^{-2}$ s$^{-1}$). These observations further corroborate that not only is the wind persistent but also extremely variable, with the column density varying in the $N_{\rm H} \sim 3$–$8 \times 10^{23}$ cm$^{-2}$ range (see Braito et al. 2021; hereafter B21). Interestingly, while the XMM-Newton, NuSTAR, and Chandra observations did not detect the second faster phase (outflowing with $v_{\rm out2}/c \sim -0.2$), this component was present during the 2018 Swift observation. MCG-03-58-007 is thus a unique disk wind, whose variability can inform us on the structure of the disk winds and ultimately their driving mechanism.

The paper is structured as follows: in Section 2 we describe the new XMM-Newton and NuSTAR monitoring campaign and the data reduction, while in Section 3 we present the variability analysis and the overall spectral evolution. In Section 4 we report on the initial spectral analysis, where the disk wind is modeled adopting a grid of photoionized absorbers

**Table 1**
Summary of the XMM-Newton and NuSTAR Observations of MCG-03-58-007 Performed in 2019: Observation Number, Observatory, Start Time, Stop Time, Instrument, Elapsed and Net Exposure Times

| Obs. | Satellite | Start Date (UT Time) | Stop Date (UT Time) | Instrument | Elapsed Time (ks) | $\text{Exposure}_{(\text{net})}$ (ks)[a] |
|---|---|---|---|---|---|---|
| OBS 1 | XMM-Newton | 2019-05-14 15:05 | 2019-05-15 11:57 | EPIC-pn | 75.1 | 46.2 |
| | NuSTAR | 2019-05-14 13:36 | 2019-05-15 11:36 | FPMA/B | 78.7 | 37.7 |
| OBS 2 | XMM-Newton | 2019-05-24 03:55 | 2019-05-24 21:12 | EPIC-pn | 62.3 | 53.8 |
| | NuSTAR | 2019-05-24 03:51 | 2019-05-25 02:21 | FPMA/B | 78.7 | 40.2 |
| OBS 3 | XMM-Newton | 2019-05-28 15:37 | 2019-05-29 10:59 | EPIC-pn | 69.7 | 45.2 |
| | NuSTAR | 2019-05-28 14:16 | 2019-05-29 11:11 | FPMA/B | 78.9 | 37.4 |
| OBS 4 | XMM-Newton | 2019-06-13 15:00 | 2019-06-14 09:54 | EPIC-pn | 68.0 | 46.6 |
| | NuSTAR | 2019-06-13 08:41 | 2019-06-14 10:41 | FPMA/B | 93.1 | 40.5 (31.3[b]) |

**Notes.**
[a] The net exposure times are obtained after the screening of the cleaned event files for high background and dead time.
[b] NuSTAR cleaned exposure time of the part of the observation that overlaps with the XMM-Newton one.

generated with the XSTAR photoionization code (Kallman et al. 2004), while in Section 5 the disk wind is fitted with synthetic spectra generated from the accretion disk-wind model developed by Sim et al. (2008, 2010b). The disk-wind energetics and variability properties are presented in Section 6, where we will also discuss the overall scenario for this unique wind as inferred from the extraordinary variability it displayed in this monitoring.

Throughout the paper we assume a concordance cosmology with $H_0 = 70\,\text{km s}^{-1}\,\text{Mpc}^{-3}$, $\Omega_{\Lambda_0} = 0.73$, and $\Omega_m = 0.27$. For the abundances, we used those of Wilms et al. (2000).

## 2. Observations and Data Reduction

In 2019 MCG-03-58-007 was observed four times simultaneously with XMM-Newton and with NuSTAR (Harrison et al. 2013). The observations were part of a monitoring campaign, designed to investigate the variability of its fast disk wind. The observations were spaced apart by 5, 10, and 15 days, and we will refer to them as OBS1, OBS2, OBS3, and OBS4. In Table 1 we report the summary of the four observations.

### 2.1. XMM-Newton

The XMM-Newton-EPIC instruments operated in full frame mode and with the thin filter applied. We processed and cleaned the XMM-Newton data using the Science Analysis Software (SAS, ver. 16.0.0; Gabriel et al. 2004) and the resulting spectra were analyzed using standard software packages (FTOOLS ver. 6.27.2, Blackburn 1995; XSPEC ver. 12.11, Arnaud 1996). The EPIC data were first filtered for high background, which affected most of the observations. The EPIC-pn source and background spectra were extracted using a circular region with a radius of 32″ and two circular regions with a radius of 28″, respectively. We generated the response matrices and the ancillary response files at the source position using the SAS tasks *arfgen* and *rmfgen* and the latest calibration available. For the scientific analysis reported in this paper, we concentrated on the pn data, which have the highest signal-to-noise ratio in the 2–10 keV band. The pn source spectrum was binned to have at least 50 counts in each energy bin. For each of the observations, we also extracted light curves in the 3–6 keV and 7–10 keV energy bands.

### 2.2. NuSTAR

All the NuSTAR observations of MCG-03-58-007 were coordinated with XMM-Newton, starting before each XMM-Newton observation and ending just after. For all the observations, we considered the whole NuSTAR exposure with the exception of OBS4, where not only did the NuSTAR observation start several hours before the XMM-Newton one, but MCG-03-58-007 was also in a relatively brighter state at the beginning of this observation (see Figure 1). In this case, only the portion of the NuSTAR observation that overlaps with XMM-Newton was considered. We reduced the NuSTAR data following the standard procedure using the HEASOFT task NUPIPELINE (version 0.4.6) of the NuSTAR Data Analysis Software (NUSTARDAS, ver. 1.8.0). We used the calibration files released with the CALDB version 20170727 and applied the standard screening criteria, where we filtered for the passages through the South Atlantic Anomaly (SAA) setting the mode to "optimized" in NUCALSAA. For each of the focal plane modules (FPMA and FPMB), the source spectra were extracted from a circular region with a radius of 46″, while the background spectra were extracted from two circular regions with a 46″ radius located on the same detector. Light curves in different energy bands were extracted from the same regions using the NUPRODUCTS task. The FPMA and FPMB background-subtracted light curves were then combined into a single one. After checking for consistency, we combined the spectra and responses from the individual FPMA and FPMB detectors into a single spectrum. The spectra were then binned to at least 50 counts per bin and fitted over the 3–40 keV energy range.

## 3. The XMM-Newton and NuSTAR Light Curves

In the previous observations, MCG-03-58-007 displayed a remarkable variability both on short and long timescales (B18, M19 and B21); in particular, in the NuSTAR observation performed in 2015, we witnessed a rapid occultation event due to a possible increase in the opacity of the wind (B18). We therefore first inspected the light curves extracted for each observation. In Figure 1 we report the NuSTAR light curves extracted with a bin size of 5814 s, which corresponds to the NuSTAR orbital period. In the top three panels, we show the

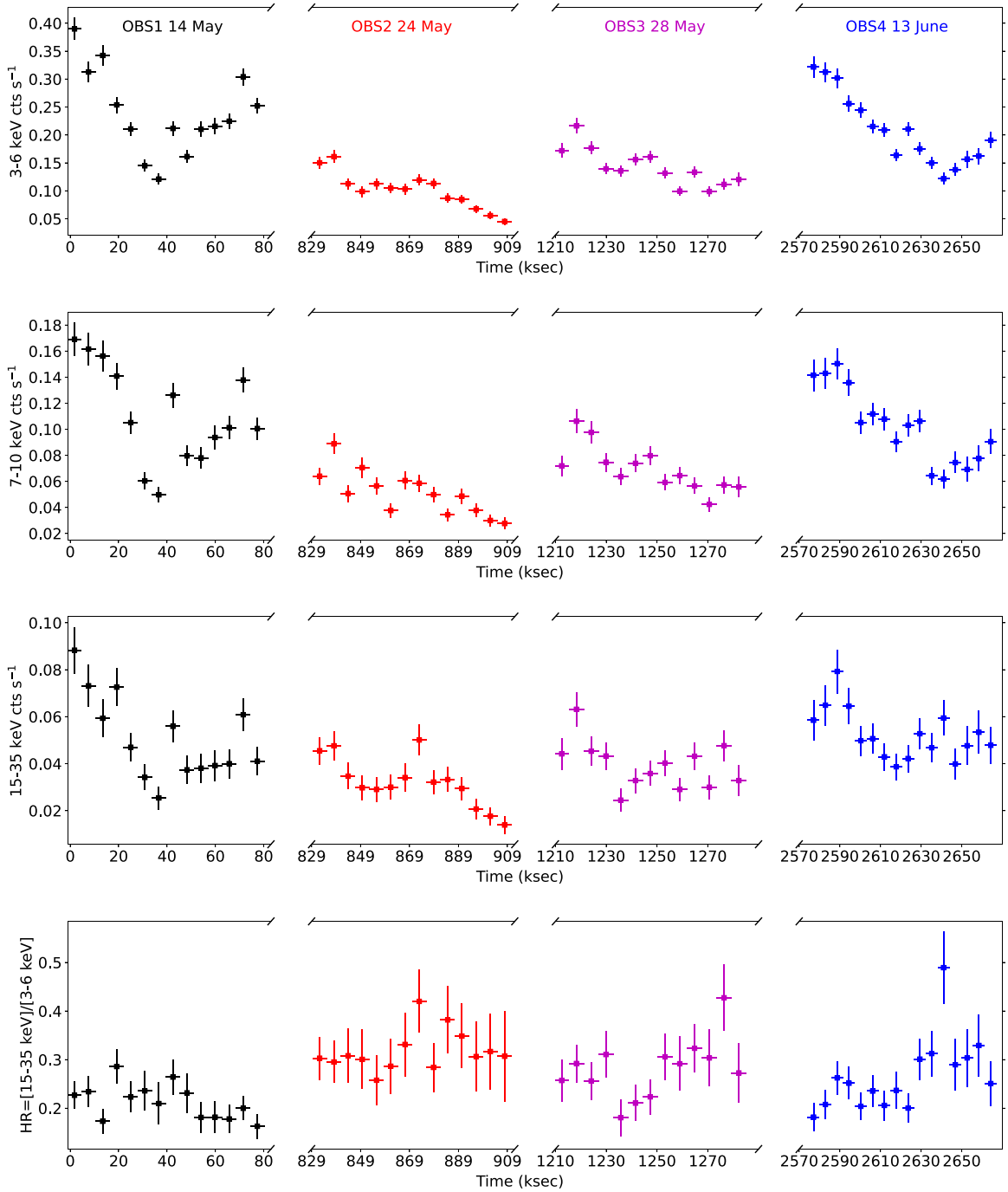


**Figure 1.** NuSTAR light curves (extracted with a bin size of 5814 s) and hardness ratio for the four observations, where OBS1, OBS2, OBS3, and OBS4 are shown in black, red, magenta, and blue, respectively. From top to bottom, we show the curves extracted in the 3–6 keV (upper panel), in the 7–10 keV (second panel), and in the 15–35 keV energy bands (third panel). The lower panel reports the $HR_{\rm NuSTAR}$ light curve, where the $HR_{\rm NuSTAR}$ was defined as $CR_{15-35{\rm keV}}/CR_{3-6{\rm keV}}$. All the light curves show a degree of variability during each of the observations, in particular in the lower-energy bands. On the contrary, the $HR_{\rm NuSTAR}$ is less variable on short timescales, but it clearly varies between the different observations.

light curves extracted in the 3–6 keV, 7–10 keV, and 15–35 keV energy bands, while in the bottom panel, we show the hardness ratio (defined as $HR_{\rm NuSTAR} = CR_{15-35{\rm keV}}/CR_{3-6{\rm keV}}$) as a function of time. The three bands were chosen to sample the spectral components that were previously seen in the X-ray spectra of MCG-03-58-007 (see M19 and B21). The 3–6 keV samples the curvature imprinted by the fully covering absorber, the 7–10 keV band covers the energy range where the absorbing features ascribed to the fast wind have been detected, and the 15–35 keV covers the primary continuum. Similarly, we extracted the EPIC-pn light curves in the 3–6 keV and in the 7–10 keV bands with a bin size of 1000 s; these are shown in Figure 2, together with the relative hardness ratio (defined as $HR_{XMM} = CR_{7-10{\rm keV}}/CR_{3-6{\rm keV}}$).

The inspection of the light curves shows that MCG-03-58-007 varies rapidly in all the energy bands. For example, in OBS1, all the count rates vary for more than a factor of three on timescale as short as tens of kiloseconds. However these variations do not appear to be accompanied by a fast variability of the hardness ratios. According to the light curves, OBS1 and

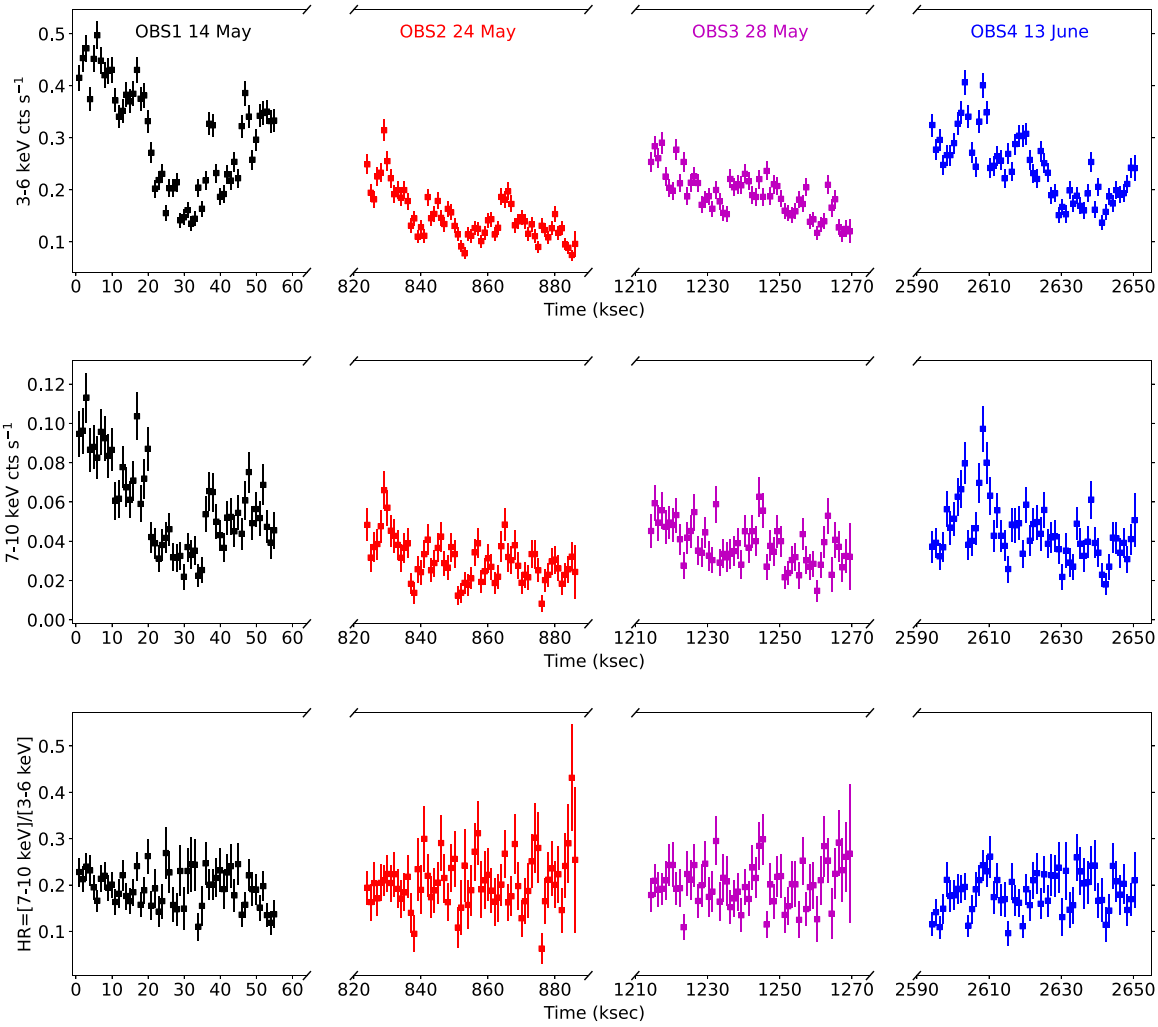


**Figure 2.** EPIC-pn light curves and hardness ratio for the four observations where: OBS1, OBS2, OBS3, and OBS4 are shown in black, red, magenta, and blue, respectively. The light curves were extracted with a bin size of 1000 s. The upper panel reports the 3–6 keV light curve, while the middle panel shows the 7–10 keV light curve. MCG-03-58-007 displays a remarkable variability in each of the observations. In the lower panel, we report the $HR_{\rm XMM}$ light curve; here the $HR_{\rm XMM}$ was defined as $CR_{7-10\rm keV}/CR_{3-6\rm keV}$. We note that despite the strong flux variability, there is no clear $HR_{\rm XMM}$ variability. This implies that the overall spectral curvature between 3 and 10 keV remains roughly the same during the whole campaign.

OBS2 caught MCG-03-58-007 in the brightest and the faintest state, respectively. The $HR_{\rm XMM}$, which tracks the 3–10 keV spectral curvature, does not vary between the observations (see Figure 2, lower panel), suggesting that the overall spectral shape between 3 and 10 keV is similar in all the observations. Conversely $HR_{\rm NuSTAR}$, which tracks the variability of the spectral curvature with respect to the primary continuum, varies between all the observations (see Figure 1, lower panel). On short timescales, $HR_{\rm NuSTAR}$ exhibits only small fluctuations, where the only possible change is seen in OBS3 and OBS4, when MCG-03-58-007 becomes marginally harder at the end of the observations.

In order to quantify the source variability, we calculated, for each band and detector, the "excess variance" (Edelson et al. 2002; Vaughan et al. 2003), which is defined as $\sigma^2_{\rm XS}= S^2 - \overline{\sigma^2_{\rm err}}$, where $S^2 = \frac{1}{N-1}\sum_{i=1}^{N}(x_i - \overline{x})^2$ is the sample variance, $\overline{\sigma^2_{\rm err}}$ is the mean square error defined as $\overline{\sigma^2_{\rm err}} = \frac{1}{N}\sum_{i=1}^{N}\sigma^2_{\rm err,i}$, $x_i$ and $\sigma_{\rm err,i}$ are the observed values and the uncertainties on each individual measurement, respectively. From these we can then calculate the fractional rms variability amplitude, defined as $F_{\rm var} = \sqrt{\frac{\sigma^2_{\rm XS}}{\overline{x}^2}}$, which provides the rms variability amplitude as a percentage. In Table 2 we list the arithmetic mean $\overline{x}$ and $F_{var}$ and their uncertainties for each of the light curves. We note that the fractional variability is high in all the observations and almost independent on the selected energy band. For example, in the 7–10 keV energy band, the pn light curves are characterized by an $F_{\rm var}$ that ranges from ∼19% (OBS3) to ∼36% (OBS1). We also note that the variability is present in all the observations regardless of the observed flux, where both the brightest state (OBS1) and the faintest one (OBS2) show a similar level of variability.

## 4. Broadband Spectral Analysis

We performed all the spectral fits with XSPEC (ver. 12.11), and we included in all the models the Galactic absorption in the direction of MCG-03-58-007 ($N_{\rm H} = 1.9 \times 10^{20}$ cm$^{-2}$; HI4PI Collaboration et al. 2016), modeled with the Tuebingen—Boulder absorption model (TBABS component in *XSPEC*; Wilms et al. 2000). We used $\chi^2$ statistics, and the errors are quoted at the 90% confidence level for one interesting

**Table 2**
Light Curves Analysis

| Obs. | $CR_{3-6\ \mathrm{keV}}$ | $F_{VAR_{3-6}}$ | $CR_{7-10\ \mathrm{keV}}$ | $F_{VAR_{7-10}}$ | $CR_{15-35\ \mathrm{keV}}$ | $F_{VAR_{15-35}}$ |
|---|---|---|---|---|---|---|
| OBS1-pn | $0.302 \pm 0.003$ | $0.329 \pm 0.009$ | $0.058 \pm 0.001$ | $0.356 \pm 0.021$ | ... | ... |
| OBS2-pn | $0.148 \pm 0.002$ | $0.300 \pm 0.012$ | $0.030 \pm 0.001$ | $0.273 \pm 0.029$ | ... | ... |
| OBS3-pn | $0.191 \pm 0.002$ | $0.202 \pm 0.012$ | $0.038 \pm 0.001$ | $0.189 \pm 0.028$ | ... | ... |
| OBS4-pn | $0.247 \pm 0.002$ | $0.252 \pm 0.010$ | $0.045 \pm 0.001$ | $0.277 \pm 0.025$ | ... | ... |
| OBS1-FPM | $0.240 \pm 0.004$ | $0.312 \pm 0.016$ | $0.111 \pm 0.002$ | $0.330 \pm 0.023$ | $0.051 \pm 0.002$ | $0.326 \pm 0.037$ |
| OBS2-FPM | $0.101 \pm 0.002$ | $0.308 \pm 0.023$ | $0.051 \pm 0.002$ | $0.312 \pm 0.032$ | $0.032 \pm 0.001$ | $0.287 \pm 0.044$ |
| OBS3-FPM | $0.142 \pm 0.003$ | $0.223 \pm 0.021$ | $0.069 \pm 0.002$ | $0.231 \pm 0.028$ | $0.039 \pm 0.002$ | $0.210 \pm 0.041$ |
| OBS4-FPM | $0.208 \pm 0.003$ | $0.297 \pm 0.017$ | $0.102 \pm 0.002$ | $0.269 \pm 0.023$ | $0.052 \pm 0.002$ | $0.149 \pm 0.035$ |

parameter unless otherwise stated. All the parameters are given in the rest frame of MCG-03-58-007 ($z = 0.03233$; Sirressi et al. 2019), and the velocities are all relativistically corrected.[9] We fitted the EPIC-pn and NuSTAR-FPMA+FPMB (hereafter FPM) spectra jointly and considered the 0.3–10 keV and the 3.5–45 keV data for the EPIC-pn and FPM spectra, respectively. We included a multiplicative constant between the EPIC-pn and FPM spectra to account for any difference in normalization due to cross-calibration; this was allowed to vary, and in all the fits, we found that it ranges between $1.01 \pm 0.03$ (OBS2) and $1.12 \pm 0.02$ (OBS1).

### 4.1. The Overall Spectral Shape

In Figure 3, we show the EPIC-pn (upper panel) and NuSTAR-FPM (lower panel) fluxed spectra of all four observations. The fluxed spectra are obtained by unfolding the data against a power-law model with $\Gamma = 2$. As already noted with the previous observations of MCG-03-58-007 (B21), the soft X-ray emission and the 2–6 keV spectral curvature, which we can ascribe to the presence of the distant and neutral or low ionization absorber, do not vary. Conversely, although all the observations show absorbing structures at $E > 7$ keV, the depth of these features varies between the observations. In particular, they are deeper in OBS2 (red spectra in Figure 3) and in OBS3 (magenta spectra in Figure 3) with respect to OBS1 and OBS4, with OBS1 showing the shallower structures. Finally, as shown in Figure 3 (lower panel), above 15 keV, where the primary continuum emerges, the NuSTAR data show that this clearly varies between the observations. In particular, while during OBS1 and OBS4, MCG-03-58-007 was almost at the same intrinsic flux level, OBS2 and OBS3 are characterized by a lower level of the primary emission. This could already be anticipated by the inspection of the light curves extracted in the 15–35 keV energy range, where the mean varied from $0.051 \pm 0.002$ cts $s^{-1}$ in OBS 1 to $0.032 \pm 0.001$ cts $s^{-1}$ in OBS 2 (see Table 2).

In Figure 4, we show a zoom into the 4–10.5 keV (rest frame) EPIC-pn (upper panel) and NuSTAR (lower panel) spectra, which nicely show the changes in the absorbing structures. Here, at the beginning of this new observational campaign the absorbing structure is clearly shallower, while a broad and deep absorption trough is present at around 8 keV in the second and third observations (red and magenta spectra in the upper and lower panels of Figure 4) and at around ~7.5 keV in the last one.

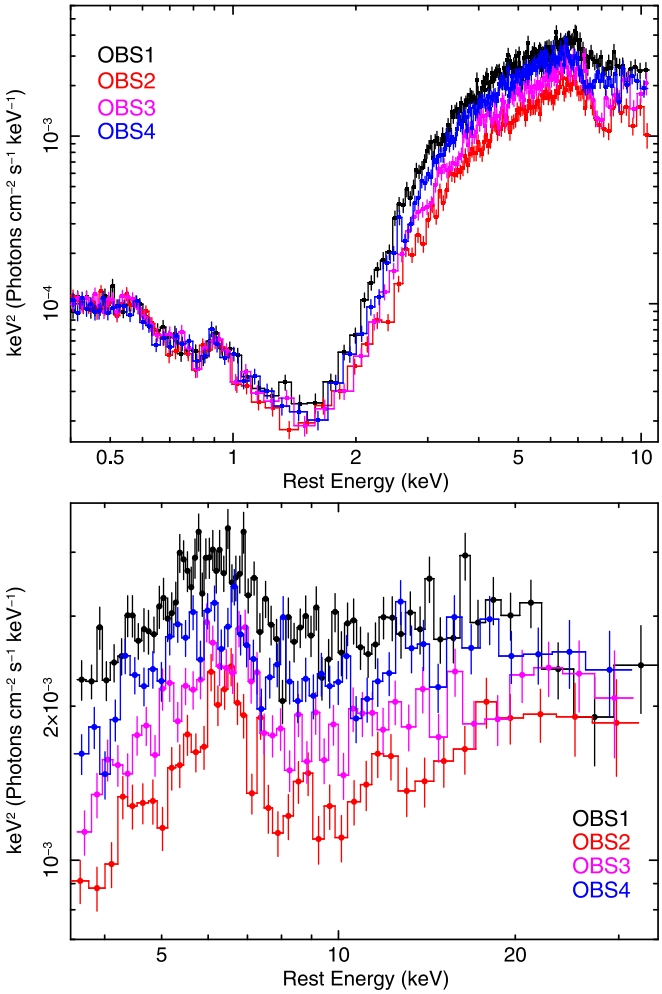


**Figure 3.** Upper panel: broadband (rest frame 0.4–10.5 keV) XMM-Newton spectra of the four observations of MCG-03-58-007 performed in 2019. The $EF_E$ spectra are obtained unfolding the data against a simple power-law model with $\Gamma = 2$. No variability is present below 2 keV, where the emission is dominated by the scattered component, while clear variability is present at higher energies, where MCG-03-58-007 dropped in flux during the OBS2. During OBS3, MCG-03-58-007 was in a slightly brighter state, but with an absorption structure almost as deep as in OBS2. Lower panel: NuSTAR spectra of the same observations. Like for the XMM-Newton data, the spectra are plotted against a simple $\Gamma = 2$ power-law model. The NuSTAR data independently confirms the presence of the deep absorption structures.

Notably, all these variations occur on relatively short timescales; while MCG-03-58-007 was brighter in OBS1, 10 days later (OBS2) it becomes clearly fainter and harder, with a possibly stronger wind. After just over 4 days, the intrinsic flux increases, and the wind appears to be as strong as in OBS2;

[9] Velocities are corrected with the relativistic Doppler formula: $v/c = [(1 + z_o)^2 - 1]/[(1 + z_o)^2 + 1]$, where $z_o$ is the measured rest-frame blueshift.

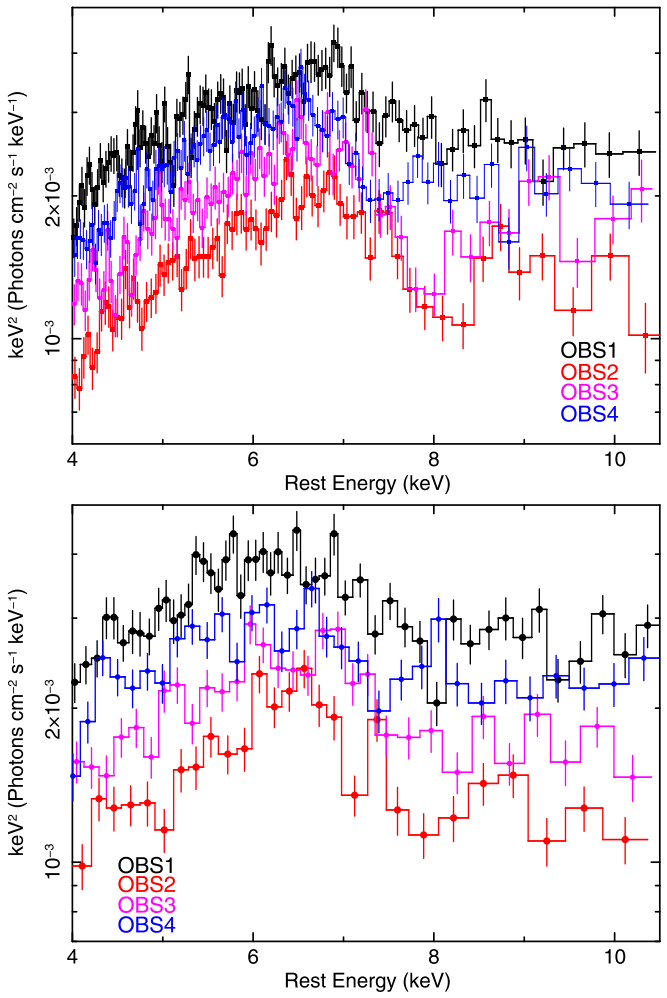


**Figure 4.** Upper panel: zoom into the EPIC-pn 4–10.5 keV (rest-frame) energy range, showing the different profile of the absorption structure seen in the 8–10 keV energy range. The $EF_E$ spectra are obtained unfolding the data against a simple power-law model with $\Gamma = 2$. Lower panel: analogous zoom into the NuSTAR spectra in the 4–10.5 keV energy range. The structures are less pronounced during OBS1 and dramatically increase in depth during the OBS2, which was performed 10 days later. Both OBS2 and OBS3 show two deep absorption troughs at ∼8 and ∼10 keV. OBS4 caught MCG-03-58-007 almost at the same flux level of OBS1, but with a different profile of the absorption structure, with the low-energy feature now at ∼7.5 keV.

then, after two more weeks, MCG-03-58-007 is almost at the same flux level of OBS1. Intriguingly, in OBS4 the absorbing structure appears to be at a lower energy with respect to all other observations.

### 4.2. The Broadband Baseline Model

We then proceeded to fit all the observations with a baseline continuum model and considered all four observations simultaneously. We first ignored the energy range where the Fe-K emission line is expected and where the absorbing troughs are present; namely, we ignored the data in the 6–15 keV energy range. Following the results obtained with the previous observations (see B21), we initially tested a neutral absorber (model ZPHABS in XSPEC) to account for the 1.5–6 keV curvature. However, this simple neutral absorber cannot fully reproduce the spectral shape between 1.5 and 3 keV, leaving some positive residuals, which suggests that the absorber could be mildly ionized and thus more transparent at those energies. We thus considered a fully covering ionized absorber. This latter was modeled with a multiplicative grid of photoionized absorbers generated with the XSTAR photoionization code (Kallman et al. 2004). We adopted a grid that has a low turbulence velocity ($v_{\rm turb} = 200\,{\rm km\,s^{-1}}$) and covers a wide range of ionization states ($\log(\xi/{\rm erg\,cm\,s^{-1}})$ between −3 and 6). The form of the baseline model is:

$$F(E) = {\rm TBABS} \times [{\rm ZPOW_{scatt}} + {\rm Gauss_{Soft}} + {\rm MEKAL} + {\rm XSTAR_{LOW}} \times {\rm ZPOW}]$$

where all the emission components are absorbed by the Galactic absorption (modeled with TBABS; $N_{\rm H} = 1.9 \times 10^{20}$ cm$^{-2}$; HI4PI Collaboration et al. 2016). For the primary emission (ZPOW), we allowed both the normalization and the photon index to vary between the observations. We allowed the $N_{\rm H}$ of the ionized absorber ($\rm XSTAR_{LOW}$) to vary, but we assumed that it has the same ionization state in all four observations. For the soft X-ray emission, the baseline model includes both the emission from a collisionally ionized plasma (MEKAL component in XSPEC; Mewe et al. 1985; with $kT = 0.13 \pm 0.01$ keV) and an additional Gaussian emission line ($\rm Gauss_{Soft}$) at $E = 0.92 \pm 0.01$ keV. As there is no evidence of variability of the soft X-ray emission, we tied all its parameters between the four observations. As noted in previous works (M19, B21), when the photon index of the scattered component ($\rm zpow_{scatt}$) is allowed to vary, it tends to a high value ($\Gamma_{\rm soft} = 3.3 \pm 0.1$).

Although simplistic, this model can reproduce the overall spectral shape ($\chi^2/\nu = 1276.6/1276$, excluding the 6–15 keV energy range). We found that both the photon indices and normalizations of the primary power-law component ($N_{\rm PL}$) vary across the monitoring campaign. For example, in OBS1 we measure $\Gamma = 2.55 \pm 0.05$ and $N_{\rm PL} = (1.3 \pm 0.1) \times 10^{-2}$ ph cm$^{-2}$ s$^{-1}$ keV$^{-1}$, while in the harder and faint state (OBS2), we derive $\Gamma = 2.22 \pm 0.06$ and $N_{\rm PL} = (3.8 \pm 0.4) \times 10^{-3}$ ph cm$^{-2}$ s$^{-1}$ keV$^{-1}$. Conversely, as seen in the previous observations, the absorber responsible for the 3–6 keV curvature does not vary between the observations with an average column density of $N_{\rm H} \sim 8.3 \times 10^{22}$ cm$^{-2}$. The ionization state is $\log(\xi/{\rm erg\,cm\,s^{-1}}) = 0.31 \pm 0.02$.

In Figure 5, we show the resulting pn and FPM spectra unfolded against this baseline model where we included the data in between 6 and 15 keV. As shown in Figure 6, where we report the residuals (plotted in terms of data-model/error) to this initial baseline continuum model, a clear deficit of counts is present above 7 keV in all of them. In particular, a strong Fe-K absorption structure is clearly visible at ∼8 keV in the first three observations and at ∼7.5 keV in the last observation. If associated with Fe XXVI ($E_{\rm Lab} = 6.97$ keV), the inferred outflow velocity is of the order of $\sim -0.14\,c$ in OBS1, OBS2, and OBS3, while in OBS4 the inferred velocity is lower and of the order of $\sim -0.07\,c$. The depth and breath of the troughs appear to be variable, where the absorption is deeper in OBS2 and OBS3 and shallower in OBS1. A second structure is clearly visible in all the residuals around ∼10–11 keV, and the structure is again more pronounced in OBS2 and OBS3. A broad excess is visible in the 6–7 keV energy range suggesting the presence of a possibly broad Fe-K emission line, while there is no evidence for a narrow Fe-K$\alpha$ emission line, which could originate from reflection off the putative parsec-scale

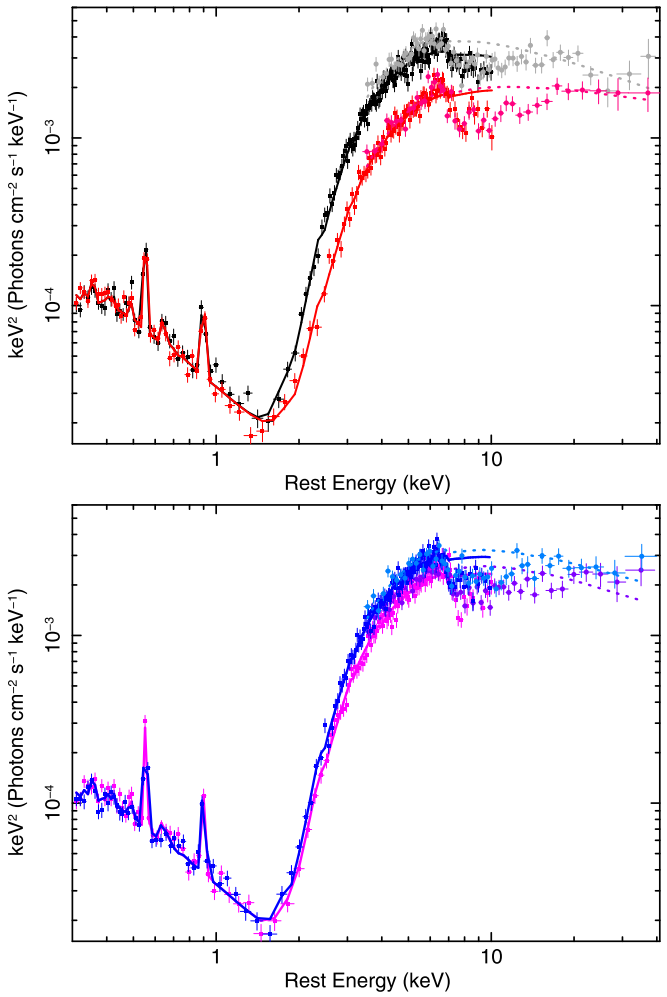


**Figure 5.** Broadband (rest-frame) pn and FPMA spectra unfolded against the baseline continuum model described in Section 4.2. Upper panel: OBS1 (pn and FPM are shown in black squares and gray filled circles, respectively) and OBS2 (pn and FPM are shown in red squares and dark red filled circles, respectively). Lower panel: OBS3 (magenta squares and purple filled circles) and OBS4 (blue squares and light blue filled circles). Here the baseline continuum model is able to account for the overall spectral shape of the X-ray emission of MCG-03-58-007.

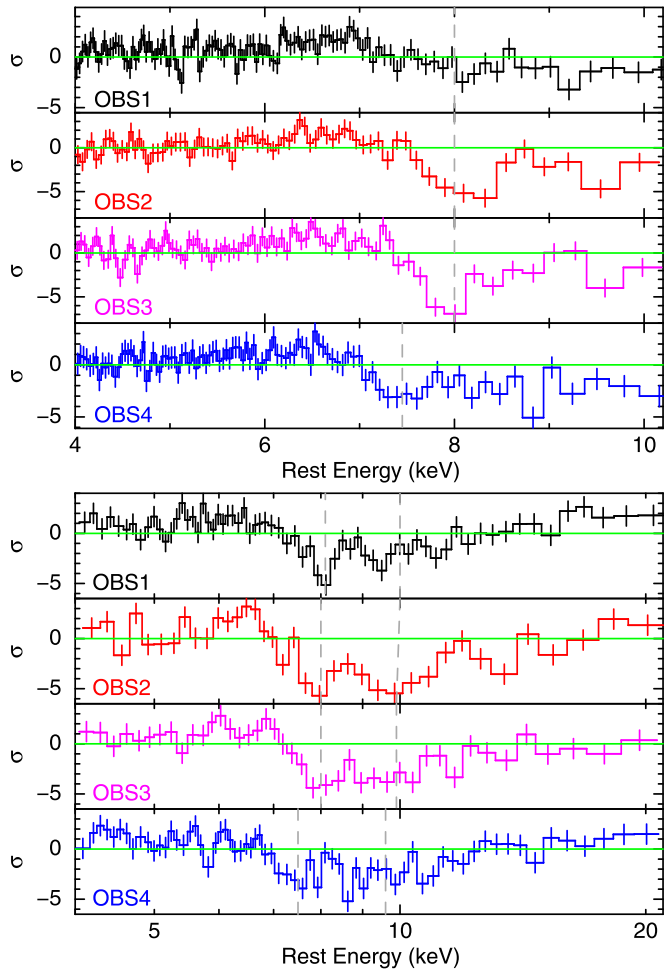


**Figure 6.** Zoom into the residuals (as data-model/error), against the baseline continuum model showing the different profiles of the absorption structures seen in the 7.5–10 keV energy range. OBS1, OBS2, OBS3, and OBS4 are shown in black, red, magenta, and blue, respectively. In the upper panel, we report the EPIC-pn 4–10 keV residuals, while the NuSTAR 4–20 keV residuals are shown in the lower panel. Absorption structures (marked with the vertical dashed lines) are present in all the observations, but they show a remarkable variability in depth and energy, whereas they are less pronounced during OBS1 and increase in depth during OBS2. A possible second structure is also visible in all the residuals at around 10 keV. This could be either associated with a higher-velocity wind phase or ascribed to a contribution from higher-order Fe-K absorption (see Sections 4.3 and 5.1).

torus. Similarly, no clear excess, that could be ascribed to a strong Compton reflection, emerges above 15 keV.

### *4.3. Photoionization Modeling of the Fe-K Absorption*

We then proceeded to fit the broadband data including both a Gaussian emission line, to account for the possibly broad Fe-K emission line, and the ionized absorber. In order to determine the optimal multiplicative grid of photoionized absorbers, we first note that the underlying continuum is similar to what we measured in the past observations, where the soft (between 0.3 and 1.2 keV) photon index is $\Gamma \sim 3$ and the hard X-ray $\Gamma$ is between 2 and 2.6. We therefore adopted an absorption grid similar to the one used by B21,[10] which was generated with XSTAR and optimized for high column density ($N_{\rm H} = 10^{22} - 2 \times 10^{24}$ cm$^{-2}$) and high ionization ($\log(\xi/{\rm erg\,cm\,s^{-1}}) = 3-7$) absorbers.

[10] To generate the grid, we used an SED similar to IZW1, where the soft (between 0.3 and 1.2 keV) photon index ($\Gamma$) is $\sim$3 and the hard X-ray $\Gamma$ is 2.2 (see Reeves & Braito 2019).

We then inspected the main absorption structures seen between $\sim$8 and 12 keV, to determine the optimal velocity broadening. To this end, we considered OBS2 and OBS3, where the absorption structures are deeper and better defined. We thus added two Gaussian absorption lines, we allowed their energy centroids and normalizations to vary between the two observations, but assumed that they have the same width. The first absorption line accounts for the low-energy trough; its energy centroid is found to be around 8 keV ($E = 8.08 \pm 0.09$ keV and $E = 8.07 \pm 0.10$ keV for OBS2 and OBS3, respectively) with an $EW$ of $-475 \pm 80$ eV in OBS2 and $-472 \pm 75$ eV in OBS3. A second Gaussian absorption line, which accounts for the residuals at $\sim 10 - 11$ keV, is detected at $E = 10.0 \pm 0.2$ keV in OBS2 ($EW = -550^{+90}_{-110}$ eV) and $E = 9.9 \pm 0.2$ keV in OBS3 ($EW = -410 \pm 90$ eV). We note that both absorption lines are highly significant with $\Delta\chi^2/\nu = 208/5$ and $\Delta\chi^2/\nu = 152/4$ for the lower- and higher-energy features, respectively. If compared to the

**Table 3**
Photoionization Modeling of the Wind

| Model Component | Parameter | OBS1 | OBS2 | OBS3 | OBS4 |
|---|---|---|---|---|---|
| Best-fit parameters for the baseline continuum[a]. | | | | | |
| Primary PL | $\Gamma$ | $2.57^{+0.04}_{-0.03}$ | $2.30^{+0.07}_{-0.04}$ | $2.37^{+0.05}_{-0.03}$ | $2.44^{+0.05}_{-0.03}$ |
| | $N_{\rm PL}$[b] | $14.0^{+1.2}_{-0.79}$ | $4.6^{+0.9}_{-0.3}$ | $6.7^{+0.9}_{-0.5}$ | $9.4^{+0.9}_{-0.5}$ |
| Absorber | $N_{\rm H}(\times10^{22}$ cm$^{-2})$ | $8.35^{+0.28}_{-0.03}$ | 8.35[c] | 8.35[c] | 8.35[c] |
| | log$\xi$ | $-0.29^{+0.01}_{-0.02}$ | $-0.29$[c] | $-0.29$[a] | $-0.29$[c] |
| Best-fit parameters for the variable $N_{\rm H}$ case. The statistics for the model is $\chi^2/\nu = 1868.5/1784$. | | | | | |
| Zone 1 | $N_{\rm H}(\times10^{23}$cm$^{-2})$ | $4.2^{+1.0}_{-0.7}$ | $7.4^{+1.6}_{-1.0}$ | $7.2^{+1.4}_{-0.9}$ | $5.3^{+1.4}_{-0.9}$ |
| | log$\xi$ | $4.90^{+0.07}_{-0.08}$ | 4.90[a] | 4.90[a] | 4.90[a] |
| | $v_{\rm out1}/c$ | $-0.154 \pm 0.015$ | $-0.153 \pm 0.012$ | $-0.157 \pm 0.011$ | $-0.077 \pm 0.013$ |
| Zone 2 | $N_{\rm H}(\times10^{23}$cm$^{-2})$ | $3.8^{+1.0}_{-0.9}$ | $7.1^{+1.6}_{-1.5}$ | $4.7^{+1.5}_{-1.1}$ | $5.3^{+1.4}_{-1.0}$ |
| | log$\xi$ | 4.90[c] | 4.90[c] | 4.90[c] | 4.90[c] |
| | $v_{\rm out1}/c$ | $-0.33 \pm 0.02$ | $-0.36 \pm 0.02$ | $-0.34 \pm 0.02$ | $-0.25 \pm 0.02$ |
| Best-fit parameters for the variable ionization case. The statistics for the model is $\chi^2/\nu = 1870.7/1787$. | | | | | |
| Zone 1 | $N_{\rm H}(\times10^{23}$cm$^{-2})$ | $9.4^{+1.4}_{-1.2}$ | 9.4[c] | 9.4[c] | 9.4[c] |
| | log$\xi$ | $5.32^{+0.11}_{-0.08}$ | $5.02^{+0.09}_{-0.09}$ | $5.10^{+0.09}_{-0.08}$ | $5.19^{+0.09}_{-0.08}$ |
| | $v_{\rm out1}/c$ | $-0.145 \pm 0.015$ | $-0.151 \pm 0.012$ | $-0.149 \pm 0.011$ | $-0.072 \pm 0.010$ |
| Zone 2 | $N_{\rm H}(\times10^{23}$cm$^{-2})$ | $8.2^{+1.2}_{-0.9}$ | 8.2[c] | 8.2[c] | 8.2[c] |
| | log$\xi$ | 5.32[c] | 5.02[c] | 5.10[c] | 5.19[c] |
| | $v_{\rm out1}/c$ | $-0.32 \pm 0.02$ | $-0.36 \pm 0.02$ | $-0.34 \pm 0.02$ | $-0.27 \pm 0.02$ |
| $F_{(2-10)\ \rm keV}$ ($\times10^{-12}$ erg cm$^{-2}$ s$^{-1}$) | | 4.9 | 2.5 | 3.2 | 4.0 |
| $F_{(10-40)\ \rm keV}$ ($\times10^{-12}$ erg cm$^{-2}$ s$^{-1}$) | | 5.5 | 3.5 | 4.3 | 5.2 |
| $L_{(2-10)\ \rm keV}$ ($\times10^{43}$ erg s$^{-1}$) | | 3.7 | 1.8 | 2.3 | 3.0 |

**Notes.**
[a] The baseline continuum model parameters are not affected by the assumption of a variable column density or ionization of the wind components.
[b] The normalizations are in units of $\times10^{-3}$ ph cm$^{-2}$ s$^{-1}$ keV$^{-1}$ at 1 keV.
[c] Denotes that the parameter was tied.

expected energy of the H-like Fe XXVI-Ly$\alpha$ line ($E_{\rm Lab} = 6.97$ keV), the measured energies of these two absorption lines would correspond to outflow velocities of $v/c \sim -0.15$ and $v/c \sim -0.34$, respectively. The profiles are, as expected from the inspection of the residuals, broadened with a best-fit width of $\sigma = 510^{+70}_{-60}$ eV, corresponding to a velocity broadening of $\sigma_{\rm v} \sim 20,\ 000$ km s$^{-1}$. Taking into account the measured broadening of the troughs, we chose a grid generated assuming a high turbulence velocity ($v_{\rm turb} = 25,\ 000$ km s$^{-1}$). However, we tested lower turbulence velocities and found that they generally resulted in a statistically worse fit.

In the previous observations of MCG-03-58-007, two multiplicative grids of ionized absorption models were required to account for all the absorption structures that were detected (see B21 and reference therein). Likewise, in this new set of observations a single photoionized outflowing absorber cannot account for both of the absorbing structures that are visible in the residuals. This is mainly due to the depth of the higher-energy feature. Precisely, if we associate the absorption line detected at $\sim$8.1 keV with Fe XXVI-Ly$\alpha$ ($E_{\rm Lab} = 6.97$ keV), blueshifted by $v = 0.15\,c$, the corresponding Fe XXVI-Ly$\beta$ ($E_{\rm Lab} = 8.25$ keV) would be blueshifted to $\sim$9.5 keV, which is almost consistent with the energy of the higher-energy feature. However, this line is expected to be weaker than the Fe XXVI-Ly$\alpha$ and not of a similar EW. However, this is a limitation of the modeling with a grid of photoionized absorbers generated with XSTAR, where the emission of the wind is not self-consistently accounted for, and crucially, the breadth of the line is purely ascribed to turbulence (see below).

We thus applied a model defined as:

$$F(E) = \text{TBABS} \times [\text{ZPOW}_{\rm scatt} + 2\ \text{GAUS}_{\rm Soft} + \text{MEKAL} + \text{FeK}\alpha + \text{XSTAR}_{\rm LOW} \times \text{XSTAR}_{\rm FeK,1} \times \text{XSTAR}_{\rm FeK,2} \times \text{ZPOW}].$$

Here, we added a Gaussian emission line to account for the Fe-K$\alpha$ emission line, two highly ionized outflowing absorbers ($\text{XSTAR}_{\rm FeK,1}$ and $\text{XSTAR}_{\rm FeK,2}$; hereafter, zone1 and zone2), and replaced the neutral absorber with a mildly ionized absorber ($\text{XSTAR}_{\rm LOW}$). We then proceed to perform a joint fit for all the observations.

As there is no evidence of variability of the soft X-ray emission, we again tied all the parameters of the soft X-ray components. We also tied the parameters of the mildly ionized absorber ($\text{XSTAR}_{\rm LOW}$) and of the Fe-K$\alpha$ emission line. The normalization and photon index of the primary emission were allowed to vary.

In order to quantify the apparent disk-wind variability and taking into account the known degeneracy between the ionization and $N_{\rm H}$, we first allowed the column densities of the two highly ionized absorbers (zone1 and zone2) to vary, while the wind ionization was assumed to remain constant and to be the same for both the zones. We also allowed the velocities of both zone1 and zone2 to vary between the

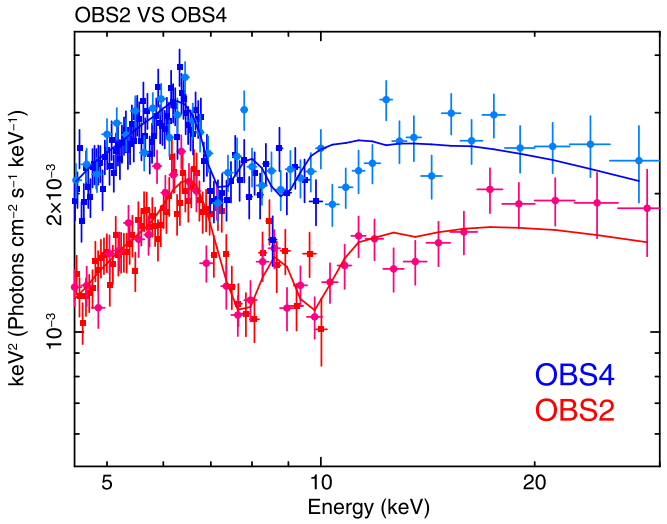


**Figure 7.** OBS2 and OBS4 spectra fitted with the best-fit XSTAR model for a variable ionization. The XMM-pn and NuSTAR data are shown with filled square and circle data points, respectively. For clarity, we show a zoom into the 4.5–30 keV energy range. OBS2 and OBS4 are representative of the two most different states observed during the monitoring campaign, where the absorption feature is at its deepest during OBS2 and slower during OBS4. The deeper absorption troughs seen in OBS2 can be accounted for by a decrease in ionization (from $\log \xi \sim 5.19$ to $\log \xi \sim 5.02$). Alternatively, the change in opacity can also be modeled by an increase of the $N_{\rm H}$ (for a constant ionization) by a $\Delta N_{\rm H} \sim 2 \times 10^{23}$ cm$^{-2}$.

observations. In Table 3, we list the results of this fit; overall, the fit statistic is good ($\chi^2/\nu = 1868.5/1784$), and only weak negative residuals are present in the 10–15 keV energy range ($\chi^2/\nu = 421.1/316$ in the 9–30 keV range). We note that both of the zones are statistically required, and removing either one of them results in much worse fits, where we have $\Delta\chi^2/\Delta\nu = 364.7/9$ for zone1 and $\Delta\chi^2/\Delta\nu = 203.2/8$ for zone2.

This model confirms that MCG-03-58-007 was caught in the intrinsically brightest state during OBS1 and in the faintest state in OBS2. During OBS3, MCG-03-58-007 starts to get brighter, and in the last observation it is almost at the same flux level of OBS1 (see Table 3). As anticipated by the inspection of the residuals, OBS1 is characterized not only by a higher intrinsic flux but also by weaker wind with $N_{\rm H\,OBS1,1} = 4.2^{+1.0}_{-0.7} \times 10^{23}$ cm$^{-2}$ and $N_{\rm H\,OBS1,2} = 3.8^{+1.0}_{-0.9} \times 10^{23}$ cm$^{-2}$ for the lower- (zone1) and higher- (zone2) velocity components of the wind. Conversely, OBS2 not only caught MCG-03-58-007 at an intrinsically low flux state, but with also a higher-density wind, where the column densities of both zones increase to $N_{\rm H\,OBS2,1} = 7.4^{+1.6}_{-1.0} \times 10^{23}$ cm$^{-2}$ and $N_{\rm H\,OBS2,2} = 7.1^{+1.6}_{-1.5} \times 10^{23}$ cm$^{-2}$, respectively. The outflowing velocities of the wind are similar in the first three observations, and they are of the order of $v_1/c \sim -0.15$ and $v_2/c \sim -0.33$, for the slow and the possibly fast components. The exception is OBS4, where both of the velocities are lower ($v_1/c = -0.077 \pm 0.013$ and $v_2/c = -0.25 \pm 0.02$) than the corresponding ones measured in the previous observations (see Table 3).

Alternatively, the change in the opacity of the wind can be parameterized by a decrease of the ionization in response to a lower intrinsic flux. In order to test this scenario, we assumed that the column density of each zone remains constant, while the ionization was allowed to vary in each of the observations; we still assumed that the two zones have the same ionization as each other. As in the previous test, we allowed the wind velocities to vary. From a statistical point of view, this model is indistinguishable from the previous one with $\chi^2/\nu = 1870.7/1787$ ($\chi^2/\nu = 423.1/319$ in the 9–30 keV range), and also in this case, there are no strong residuals. The increase of the opacity of the wind in OBS2 is now explained with a decrease of the ionization from $\log \xi = 5.32^{+0.11}_{-0.08}$ (OBS1) to $\log \xi = 5.02^{+0.09}_{-0.09}$ (see Table 3). In Figure 7, we show a comparison of Fe-K profiles, for the variable ionization case, in the two most different states observed during the campaign (OBS2 and OBS4). We can see that the deeper absorption features seen in OBS2 can be well reproduced by a decrease of the wind ionization. It is also noticeable that the profile of the absorption troughs is less blueshifted in OBS4 than in OBS2. We note that the ionization varies in proportion with the changes of the 2–10 keV luminosity, which suggest that the flow could be in photoionization equilibrium and it recombines in response to a lower luminosity of the X-ray source. Interestingly, once again we find that, while the outflowing velocities remained unchanged, within the errors, during the first three observations, they differ in OBS4. Similarly to the variable $N_{\rm H}$ model, the wind in OBS4 is slower (see Table 3). We note that in both scenarios (variable $N_{\rm H}$ or variable ionization), the wind is highly ionized, such as the observed absorption is basically always due to Fe XXVI.

## 5. The Disk-wind Model

We then proceeded to model the variable disk wind in MCG-03-58-007 with a self-consistent disk-wind model. To this end we used a table of synthetic wind spectra, which were generated using the radiative transfer disk-wind code developed by Sim et al. (2008, 2010a, 2010b). The spectral tables were computed for smooth, steady-state 2.5D[11] biconical winds. This disk-wind model treats self-consistently the absorption and re-emission from the wind and parameterizes the velocity field through the wind. Thus the spectra contain both the emission transmitted through the wind as well as the reflection or scattered emission from the wind, the latter includes also the Fe-K emission. The model also computes the ionization structure through the wind; we note that the model contains extensive atomic data and covers a wide range in ionization (for example from Fe X to Fe XXVI). The calculation is not limited to iron but it includes lighter elements as well. The wind geometry is of a biconical wind that is launched from an inner radius $R_{\rm min}$ and an outer radius $R_{\rm max}$; the wind opening angle is set by a geometrical parameter $d$, which is defined as the distance from the focus point of the wind below the origin (in units of $R_{\rm min}$). This parameter also determines the inclination of the wind with respect to the equatorial plane. A schematic view of the inner disk-wind model geometry was presented by Sim et al. (2008), and it is also reported by Reeves & Braito (2019; see their Figure 8).

As discussed in previous works, which presented and tested this disk-wind model (Sim et al. 2008, 2010a; Tatum et al. 2012; Reeves et al. 2014; Reeves & Braito 2019), an important parameter is the orientation of the observer line of sight with respect to the wind. This is defined through the parameter $\mu = \cos\theta$, where $\theta$ is the angle between the polar axis of the wind and the observer's line of sight. At low inclination angles, the observer can view directly the primary X-ray emission

[11] We refer to as 2.5D because, while the velocity field is 3D, all the other parameters (e.g., density, ionization) of the wind are axisymmetric.

without intercepting the wind; therefore, the spectra have little or no absorption. However, the computed spectra have the contribution from X-ray reflection off the surface of the wind, which also includes a broadened Fe-K$\alpha$ emission line. At higher values of $\theta$ (lower values of $\mu$), the observer's line of sight intercept more of the wind; the computed spectra contain blueshifted absorption features and also the scattered emission.

In order to model the X-ray spectra of MCG-03-58-007, we generated a grid of spectra assuming an inner launch radius of $R_{\rm min} = 64R_g$, where $R_g$ is the gravitational radius defined as $R_g = GM/c^2$ and $R_{\rm max} = 1.5R_{\rm min}$. Thus $R_{\rm min}$ corresponds to the escape radius for a wind with a terminal velocity of $v_\infty = -0.177c$. When generating the grid of spectra, we adopted $d = 1$, which, at large radii, corresponds to a wind with an opening angle of $\pm 45^\circ$ with respect to the polar axis of the wind. The model also assumes that the X-ray source is concentrated in a region of $6R_{\rm g}$ centered at the origin. We note that this disk-wind model takes into account special relativistic effects.

The synthetic wind spectra are then tabulated in a multiplicative table that can be loaded within XSPEC. The main parameters that define the wind condition are:

1. The slope of the input continuum. The continuum is set as a power law with $\Gamma$ ranging from 1.6 to 2.4 with a linear step of 0.2, calculated over the 0.1–500 keV energy range.
2. Terminal velocity. The terminal velocities are set by the choice of the inner wind radius ($R_{\rm min}$) and the terminal velocity parameter $f_{\rm v}$. This latter parameter determines the terminal velocity of the wind streamline from the escape velocity at its base with $v_\infty = f_{\rm v}\sqrt{2GM_{\rm BH}/R}$. The terminal velocity is then derived by varying the parameter $f_{\rm v}$, for the assumed launch radius of $R_{\rm min} = 64R_g$. The adopted table was generated for eight velocities with $f_{\rm v}$ ranging from 0.25 to 2.0 (in linear increments). These $f_{\rm v}$ values correspond to terminal velocities of 0.0445–0.356 $c$.
3. Inclination angle. This is defined with respect to the polar axis of the wind ($\theta$) and is parameterized via $\mu = cos\theta$. Here $\mu$ covers the 0.025–0.975 range in 20 steps (with $\Delta\mu = 0.05$). Note that, having set the opening angle to 45° for $\mu > 0.7$ (i.e., $\theta < 45^\circ$), the observer's line of sight does not intercept the wind.
4. Mass outflow rate. It is expressed in Eddington units as $\dot{M} = \dot{M}_{\rm out}/\dot{M}_{\rm Edd}$, and it covers the 0.02–0.68 range in 12 logarithmic steps. Clearly, higher $\dot{M}$ give spectra with stronger absorption and emission features.
5. Ionizing X-ray luminosity ($L_{\rm X}$). It is defined as the percentage of the 2–10 keV luminosity with respect to the Eddington luminosity ($L_{\rm X} = L_{\rm 2-10keV}/L_{\rm Edd}$). Like the mass outflow rate, it is defined in Eddington units, which makes both parameters invariant with respect to the black hole mass. The X-ray luminosity sets the ionization state of the flow, where higher values of $L_{\rm X}$ result in more ionized winds. $L_{\rm X}$ covers the 0.025%–2.5% of $L_{\rm Edd}$ in nine equally spaced logarithmic steps.

The disk-wind parameter space has been extended from previous work (e.g., Reeves et al. 2014; Reeves & Braito 2019), and hence the table grid is now composed of 86,400 synthetic spectra with the free parameters described above ($\Gamma$, $f_{\rm v}$, $\mu$, $\dot{M}$, and $L_{\rm X}$; G. Matzeu et al. 2021, in preparation). We note that, when fitting within XSPEC, the best-fit parameters and errors are determined through interpolation, if they fall in between two grid points.

### 5.1. Application of the Disk-wind Model

We then applied the disk-wind model to the four observations, replacing the two XSTAR grids and the Fe-K$\alpha$ emission line with the DISKWIND table. As per the photoionization modeling, we tied all the parameters of the soft X-ray emission and of the low ionization absorber. For the diskwind component, we tied the inclination angle, as it is unlikely that the inclination of the wind changes dramatically between the observations, especially when we consider that they are relatively close in time. The photon index, the mass outflow rate, the terminal velocity ($f_{\rm v}$), and the normalization of the primary power-law continuum were all allowed to vary. Regarding the ionizing X-ray luminosity ($L_{\rm X}$), it was allowed to vary for the first observation, while for the remaining three observations, we assumed it rescales with the normalization of the primary power law.

In Table 4, we summarize the results of the diskwind fit. We note that the model is able to reproduce the data and it returns a fit statistic of $\chi^2/\nu = 1881.8/1792$. If we consider the energy range where the wind imparts its structures (7–30 keV), the fit clearly improves returning a $\chi^2/\nu = 411.3/324$, while the XSTAR model resulted in a $\chi^2/\nu = 423.9/319$ (variable ionization case). Even more striking is the improvement above 9 keV; here the fit with the XSTAR model returned, in the 9–30 keV range, a $\chi^2/\nu = 206.0/133$ (variable ionization case), while the DISKWIND model returns $\chi^2/\nu = 170.2/138$. This is mainly explained by the better modeling of the continuum curvature between 9 and 30 keV (see below).

We determined $\mu = 0.51^{+0.02}_{-0.01}$, corresponding to an inclination angle of $\sim 60^\circ$; thus our line of sight goes through the outflow and intercepts the inner streamlines of the wind. The terminal velocities that we derived with the diskwind model confirm that during OBS4, the wind appears to be slower with respect to the first three observations; the terminal velocity measured in OBS4 is $v_{\infty,4} = -0.074^{+0.014}_{-0.010}c$, while in OBS1, OBS2, and OBS3 it is of the order of $v_\infty \sim -0.2c$ (see Table 4). Thus the difference in the measured outflow velocities does not depend on the model assumed to fit the absorption structures. In Figure 8, we show the diskwind fit to OBS2 and OBS4. Two main things emerge with respect to the analogous Figure 7: first of all, we note that the diskwind model is able to account for the emission as well as the absorption at Fe-K; second, a single diskwind component is now able to account for the higher-energy absorption structures. Several aspects of the diskwind model can explain this result. The main one is that the breadth of the absorption features is not simply due to a microturbulence velocity, but it reflects the range of velocities that our line of sight intercepts. A second important factor is that the diskwind model self-consistently includes the emission from the wind, both the scattered emission and the Fe-K emission lines. Here, the underlying continuum at $E \sim 10$ keV is different with respect to the XSTAR-grid model, because it incorporates the emission reflected off the surface of the disk wind, which adds some extra curvature between 10 and 30 keV. Furthermore, both the Fe XXVI-Ly$\alpha$ and Fe XXVI-Ly$\beta$ absorption features are accompanied by the corresponding emission lines. In other words, the apparent high EW of the higher-energy absorption feature, which drives the requirement of a second outflowing absorber

**Table 4**
Disk-wind Model: The Statistics for the Model Is $\chi^2/\nu = 1881.8/1792$

| Model Component | Parameter | OBS1 | OBS2 | OBS3 | OBS4 |
|---|---|---|---|---|---|
| | | Best-fit parameters for the baseline continuum[a] | | | |
| Primary power law | $\Gamma$ | $2.37 \pm 0.04$ | $2.14 \pm 0.04$ | $2.21 \pm 0.04$ | $2.28 \pm 0.04$ |
| | $N_{\rm PL}$[a] | $1.65^{+0.12}_{-0.12}$ | $0.66^{+0.06}_{-0.06}$ | $0.98^{+0.08}_{-0.08}$ | $1.41^{+0.13}_{-0.12}$ |
| Disk-wind parameters[c] | $\dot{M}_{\rm out}/\dot{M}_{\rm Edd}$[b] | $0.40^{+0.06}_{-0.05}$ | $0.51^{+0.05}_{-0.05}$ | $0.50^{+0.06}_{-0.06}$ | $0.19^{+0.03}_{-0.03}$ |
| | $L_{2-10}/L_{\rm Edd}$[b] | $0.63^{+0.15}_{-0.10}$ | 0.30[e] | 0.39[t] | 0.51[e] |
| | $\mu = \cos\theta$[d] | $0.51^{+0.02}_{-0.01}$ | 0.51[e] | 0.51[e] | 0.51[e] |
| | $v_\infty/c$[e] | $-0.205^{+0.009}_{-0.009}$ | $-0.210^{+0.010}_{-0.009}$ | $-0.194^{+0.009}_{-0.009}$ | $-0.074^{+0.014}_{-0.010}$ |
| $F_{(2-10)\ \rm keV}$ ($\times 10^{-12}$ erg cm$^{-2}$ s$^{-1}$) | | 4.9 | 2.5 | 3.2 | 4.0 |
| $F_{(10-40)\ \rm keV}$ ($\times 10^{-12}$ erg cm$^{-2}$ s$^{-1}$) | | 6.0 | 3.7 | 4.5 | 5.3 |
| $L_{(2-10)\ \rm keV}$ ($\times 10^{43}$ erg s$^{-1}$) | | 5.6 | 3.1 | 4.2 | 5.4 |

**Notes.**
[a] The normalizations are in units of $\times 10^{-2}$ ph cm$^{-2}$ s$^{-1}$ keV$^{-1}$ at 1 keV.
[b] Mass outflow rates in Eddington units.
[c] Percentage of the (2–10 keV) ionizing luminosity to Eddington luminosity; note that for OBS2, OBS3, and OBS4, the parameter was tied according to the ratios of the 2–10 keV fluxes.
[d] Cosine of wind inclination, with respect to the Polar axis.
[e] Denotes that the parameter was tied.

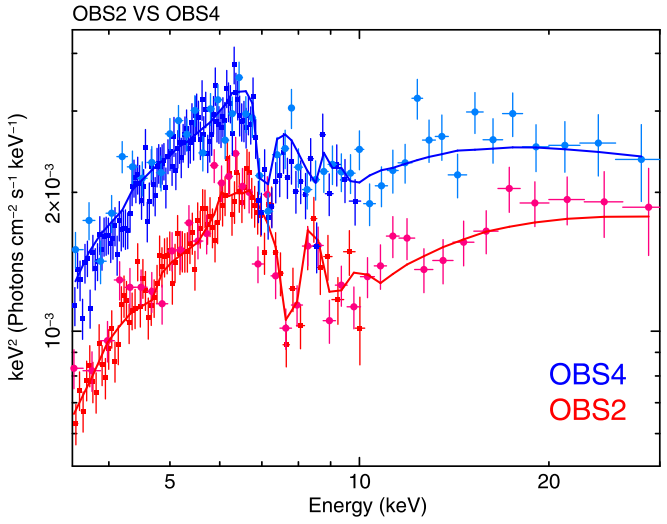


**Figure 8.** OBS2 and OBS4 spectra fitted with the disk-wind model. The XMM-pn and NuSTIn Obs 1AR data are shown with filled square and circle data points, respectively. The model can now reproduce all the Fe-K profile with a single zone. The wind terminal velocity is of $v_{\infty,2}/c = -0.21 \pm 0.01$ in OBS2 and $v_{\infty,4}/c = -0.074^{+0.014}_{-0.010}$ in OBS4. Note that the disk-wind model includes both the emission transmitted through the wind and reflected/scattered from the wind, including the Fe-K emission. It is noticeable how the model can now better reproduce the 9–30 keV data, when compared to the XSTAR model, as shown in Figure 7.

with the XSTAR model, is artificially increased by the higher level of the intrinsic continuum. The difference in the continuum can be also seen by comparing the overall best-fit obtained with the XSTAR (see Figure 7) versus and the diskwind model (see Figure 8). It is clear that the diskwind model can better reproduce the curvature in the 9–30 keV range, where the XSTAR model marginally overpredicts the observed X-ray emission. This explains the improvement in the fit statistic over the 9–30 keV range.

For OBS1, the derived ionizing X-ray luminosity is $L_{\rm X} = 0.63^{+0.15}_{-0.10}\%$ of $L_{\rm Edd}$ (for OBS1), which for a black hole mass of $\sim 10^8 M_\odot$ corresponds to a $L_{2-10\ \rm keV} \sim 6 \times 10^{43}$ erg s$^{-1}$ (see Table 4). We note that this is similar to the measured 2–10 keV luminosity, which is of the order of $\sim 5.6 \times 10^{43}$ erg s$^{-1}$. This implies that wind ionization is close to the expectation given the observed X-ray luminosity. The best-fit with the diskwind model suggests that during the first three observations, the overall properties of the disk wind of MCG-03-58-007 are rather similar. The variable wind opacity here is determined by the changes of the illuminating X-ray luminosity, which sets the wind ionization. Here the wind terminal velocities are all of $\sim -0.2c$ and the mass outflow rate is only marginally higher during OBS2 and OBS3, where it is of the order of $\dot{M} = \dot{M}_{\rm out}/\dot{M}_{\rm Edd} = 0.5 \pm 0.06$ (or 50% of Eddington), than during OBS1 ($\dot{M}_1 = 0.40^{+0.05}_{-0.06}$). Conversely, it appears that OBS4 caught a different phase or streamline of the wind, characterized by the lowest velocity and correspondingly the lowest mass outflow rate ($\dot{M}_4 = 0.19^{+0.03}_{-0.03}$).

To confirm that, we produced the contours of $\dot{M}$ versus the outflow velocity for OBS2 and OBS4, which are shown in Figure 9. It is noticeable that the wind caught in OBS4 is characterized by a much lower outflow rate and velocity than in OBS2, at a confidence greater than 99.9%. We note that a lower mass outflow rate does not imply that the wind is characterized by a lower mass load; indeed, the low value measured during OBS4 can be simply explained by the low velocity of the wind ($v_{\infty,4}/c = -0.074^{+0.014}_{-0.010}$), which is almost a factor of three lower than the velocity measured in OBS2 ($v_{\infty,2}/c = -0.210^{+0.010}_{-0.009}$). To support this explanation, we can obtain a first order estimate of the column density of the flow along the line of sight by estimating the factor by which the wind suppresses, by scattering, the 2–10 keV continuum. This in turn translates into the Compton depth of the wind and therefore into a first order estimate of its column density. For OBS2, OBS3, and OBS4, we found that the Compton depths are similar and are of the order of $\tau \sim 0.9$ for a corresponding $N_{\rm H} \sim 1.3 \times 10^{24}$ cm$^{-2}$. This confirms that the main driver for the low $\dot{M}_4$ is the lower velocity of the wind. The Compton depth is only marginally lower in OBS1, with $\tau \sim 0.7$ and

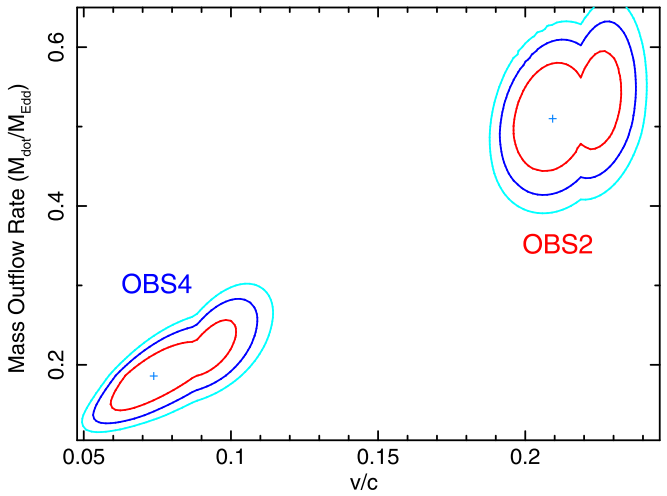


**Figure 9.** Confidence contours for the mass outflow rate versus the wind terminal velocity ($v/c$) for OBS2 (upper right contours) and OBS4 (lower left contours). The contours shown are at the 90%, 99%, and 99.9% significance levels for two interesting parameters. The best-fit values are marked with blue crosses. It is clear that the wind parameters in OBS2 and OBS4 occupy two distinct loci.

$N_{\rm H} \sim 10^{24}$ cm$^{-2}$, and may explain the slightly lower mass outflow rate.

It is worth noting that the estimates of the absorbing column densities are similar to the one derived with the photoionization modeling, where an $N_{\rm H} \sim 9.4 \times 10^{23}$ cm$^{-2}$ was inferred with the variable ionization model. More importantly, the drop in the outflow velocity in OBS4 does not depend on the assumed model, despite the differences in the physical assumptions between the models.

## 6. Discussion

### 6.1. The Energetics of the Disk Wind

Here we compare the energetics for the disk wind in MCG-03-58-007 that can be derived with the DISKWIND and with the XSTAR modeling. First of all, from the DISKWIND model, we derived that the difference in the outflow rates is driven by changes of the outflow velocity rather than changes of the mass load of the wind. Indeed, the corresponding column density is always of the order of $N_{\rm H} \sim 10^{24}$ cm$^{-2}$ and the variation in the wind opacity is explained by the changes of the ionizing X-ray luminosity ($L_{\rm X}$), which sets the ionization of the wind. Therefore, we consider the energetics derived with the XSTAR model where we allowed the ionization rather than the $N_{\rm H}$ to vary. We also consider only the slow component of the wind, because the DISKWIND model shows that the second zone could be an artifact of the modeling. We can follow the same argument described in B21, where the mass outflow rate normalized to the Eddington rate can be derived with the equation:

$$\dot{M} = \frac{\dot{M}_{\rm out}}{\dot{M}_{\rm Edd}} = 2\frac{\Omega}{4\pi}\mu_{\rm a}\, N_{\rm H}\, \sigma_{\rm T}\, \eta \left(\frac{v_{\rm out}}{c}\right)^{-1}, \quad (1)$$

which assumes a biconical geometry for the flow (Krongold et al. 2007), where $\mu_{\rm a} = n_{\rm H}/n_{\rm e} = 1.3$ for solar abundances, $\sigma_{\rm T}$ is the Thomson cross section, and $\eta = 0.1$ is the accretion efficiency. Here we also assume, following the same arguments as presented in B21, that the wind subtends a solid angle of $\Omega/4\pi = 0.5$ and that the launching radius of the wind is the escape radius ($R_{\rm min} = 2GM_{\rm BH}/v^2$), which gives the most conservative estimates of the mass outflow rate and energetics (see Gofford et al. 2013; Tombesi et al. 2012).

In OBS1, OBS2, and OBS3 the wind has $N_{\rm H} = 9.4^{+1.4}_{-1.2} \times 10^{23}$ cm$^{-2}$ and an averaged velocity of $v_{\rm out}/c = -0.148 \pm 0.013$ (see Table 3); the derived mass outflow rate is thus $\dot{M}_{\rm out\ 1,2,3}/\dot{M}_{\rm Edd} = 0.54 \pm 0.09$. Conversely, for OBS4 we derive $\dot{M}_{\rm out,4}/\dot{M}_{\rm Edd} = 1.12 \pm 0.23$, which is much higher than what is deduced from the DISKWIND fits; see below.

The kinetic power of the wind ($L_{\rm KIN} = 1/2\dot{M}_{\rm out}\, v^2_{\rm out}$) normalized to the Eddington luminosity ($L_{\rm Edd} = \eta\, \dot{M}_{\rm Edd}\, c^2$) is then:

$$\dot{E} = \frac{L_{\rm KIN}}{L_{\rm Edd}} = \frac{\Omega}{4\pi}\, \mu\, N_{\rm H}\, \sigma_{\rm T} \frac{v_{\rm out}}{c}. \quad (2)$$

Using Equation (2), the kinetic power of the wind is then $\dot{E}_{1,2,3} = 6 \pm 1\%$ of Eddington in the first three observations and $3 \pm 1\%$ in OBS4. We note that the higher value of the mass outflow rate derived for OBS4 is driven by the higher $R_{\rm min}$ ($\sim 5 \times 10^{15}$ cm), while the higher kinetic power derived for the first three observations is driven by the higher outflowing velocity.

The kinetic power and outflow rates are within the range of the measurements reported for the past observations (B18, M19, B21). In particular, the outflow rate and kinetic power measured in the first three observations are similar to the energetics measured for the phase outflowing with $v \sim -0.2\, c$ that was detected in the past Swift and Suzaku observations (see B21). On the other hand, the mass outflow rate and kinetic power measured in OBS4 are close to the energetics measured for the slow component of the wind as seen in the Suzaku observation, where we measured $\dot{M}_{\rm out}/\dot{M}_{\rm Edd} \sim 0.84$ and $\dot{E} \sim 2.5\%$. However, a strong assumption in these and in the past estimates of the energetics of the wind is that the wind is launched at the escape radius, which may not be correct. Indeed, as we will discuss below, it is implausible that the launching radius changes so dramatically, from $R_{\rm min} \sim 10^{15}$ cm (or $\sim 50 R_{\rm g}$ as inferred for OBS1, OBS2, and OBS3) to $\sim 5 \times 10^{15}$ cm (or $\sim 350 R_{\rm g}$ as measured in OBS4), in $\sim$16 days and the most plausible scenario is that the wind always originates at the same distance from the black hole.

This limitation is not present in the diskwind model, where the wind streamline is launched from a fixed innermost radius $R_{\rm min} = 64 R_{\rm g}$ and an outer radius of $1.5 R_{\rm min}$, and the terminal velocity of the wind does not have to be at the exact escape velocity at the innermost radius. In Table 5 we report the mass outflow rate, terminal velocity, kinetic power, and momentum rate of the wind for each of the observations. We note that since the wind streamline has a physical extent, determined by $R_{\rm min}$ and $R_{\rm max}$, it also has a range of terminal velocities. The terminal velocities and energetics reported in Table 5 are derived for $R_{\rm min}$ ($v_\infty = f_{\rm v}\sqrt{2GM_{\rm BH}/R_{\rm min}}$). However, if we assume the mean launch radius and its mean velocity[12], the kinetic power and momentum rate would be only a factor of 20% and 10% lower, respectively. We found that the mass outflow rate ranges between 40% and 50% of Eddington for the first three observations, while it is lower in OBS4 and of the order of $\dot{M}_4 = 19 \pm 3\%$. The lower value of $\dot{M}_4$ reflects the much

[12] This is the mean between the terminal velocity at the inner launching radius (i.e., $64 R_{\rm g}$) and the velocity at the outer radius of $96 R_{\rm g}$.

**Table 5**
Outflow Energetics Derived with the Disk-wind Model

| | OBS1 | OBS2 | OBS3 | OBS4 |
|---|---|---|---|---|
| $\dot{M}_{\rm out}$[a] | $0.40^{+0.05}_{-0.06}$ | $0.51^{+0.05}_{-0.05}$ | $0.50^{+0.06}_{-0.06}$ | $0.19^{+0.03}_{-0.03}$ |
| $v_\infty/c$[b] | $-0.205^{+0.009}_{-0.009}$ | $-0.210^{+0.010}_{-0.009}$ | $-0.194^{+0.009}_{-0.009}$ | $-0.074^{+0.014}_{-0.010}$ |
| $\%\dot{E}$[c] | $9 \pm 2$ | $11 \pm 2$ | $9 \pm 1$ | $0.5 \pm 0.2$ |
| $\dot{p}$[d] | $0.82 \pm 0.14$ | $1.07 \pm 0.14$ | $0.97 \pm 0.15$ | $0.14 \pm 0.05$ |

**Notes.**
[a] Mass outflow rates in Eddington units.
[b] Mean wind velocity; see Sections 5 and 6.1 for details.
[c] Percentage outflow kinetic power in Eddington units.
[d] Outflow momentum rate in Eddington units.

lower velocity of the wind in OBS4. As we discussed in Section 5.1, the difference in the derived mass outflow rates does not imply a different mass load of the wind between the four observations, but rather it depends on the drop in velocity in OBS4 from $v_{\infty,1,2,3}/c \sim -0.2$ to $v_{\infty,4}/c \sim -0.07$. Indeed, in Section 5.1 we showed that during the monitoring, the column density of the flow along the line of sight is almost constant and of the order of $\sim 1.3 \times 10^{24}$ cm$^{-2}$. The derived kinetic power of the wind ranges between 0.5%–10% of Eddington, which, for a black hole mass of $\sim 10^8 M_\odot$ (as estimated by B18), corresponds to $L_{\rm KIN} \sim 6 \times 10^{43} - 10^{45}$ erg s$^{-1}$. Similarly to the mass outflow rate results, the lower value of $\dot{E}_4$ ($0.5 \pm 0.2\%$) reflects the lower velocity of the wind in the last observation.

We can now compare these more robust estimates of the disk-wind kinematics with the energetics of the possible kiloparsec-scale molecular outflow detected in the ALMA observation ($\dot{E}_{\rm CO} \sim 10^{42}$ erg s$^{-1}$, $\dot{p}_{\rm CO} \sim 8 \times 10^{34}$ g cm s$^{-2}$; Sirressi et al. 2019). We confirm that we do not detect a boost of the momentum rate of the putative molecular outflow compared to the X-ray disk wind. Instead, the momentum rates of the two outflows are consistent. Furthermore, the kinetic power of the disk wind is still well above the kinetic energy carried by the molecular gas phase. Precisely, even if we consider the lowest $\dot{E}$ of OBS4, we still obtain that $\dot{E}_{\rm CO}/L_{\rm KIN}$ is $\sim 0.02$.

This result does not imply that the disk wind in MCG-03-58-007 does not have an impact on the host galaxy, but it may simply reflect a lower efficiency in coupling with the host galaxy gas (see a recent review by Veilleux et al. 2020). Lower efficiencies in transferring the kinetic energy to the large-scale molecular gas, like the one measured for MCG-03-58-007, have now been inferred for several powerful disk winds (Mizumoto et al. 2019), among them, some of the most powerful disk winds, like PDS 456 and IZW1 (Bischetti et al. 2019; Reeves & Braito 2019). The lack of an energy-conserving outflow can also be a sign that the central SMBH has not reached its critical M–$\sigma$ mass; in this case, the momentum that can be imparted by the ultra-fast disk wind is not enough to sweep the gas up to the cooling radius, where the wind shock no longer cools. In this case the wind will not be able to expand adiabatically, as in an energy-conserving outflow. The outflow will eventually fall back, because its momentum is not enough to carry the weight of the gas that it has swept up (see King 2003, 2005; King & Pounds 2015).

Critically, our analysis shows how challenging it is to compare the energetics of the large-scale outflows and the ultra-fast disk winds. Indeed, according to the disk-wind model, the kinetic power of the wind in MCG-03-58-007 changes by more than an order of magnitude on a timescale as short as a month. Therefore, as already pointed out in other works (Nardini & Zubovas 2018; Zubovas & Nardini 2020), the energetics derived with single-epoch observations may be highly inaccurate, because they may not reflect the typical kinetic power of the wind. A single observation determines the disk-wind properties at a specific time, while disk winds are generally extremely variable, as demonstrated by multi-epoch observations of the best examples of winds (e.g., PDS 456, Reeves et al. 2018a; Matzeu et al. 2017; IRASF 11119+3257, Tombesi et al. 2017; PG 1211+143, Reeves et al. 2018b; APM 08279+5255, Saez & Chartas 2011). A second, but no less important, aspect that could have a profound impact when comparing these energetics is that, unlike with XSTAR, the DISKWIND model provides a self-consistent estimate of the energetics. For example, the kinetic output measured for OBS4 with the XSTAR and the DISKWIND models differs by almost an order of magnitude.

### 6.2. The Location of the Disk Wind

We can now place some constraints on the location and size scale of the streamline of the wind by means of its variability. The component of the disk wind that is outflowing with $v_{\rm out} \sim -0.2\,c$ lasts at least for the first three observations (see Tables 3 and 4), which cover a timescale of 14 days (see Table 1). From this we can derive that the size scale of this absorber is $\Delta R = v \times \Delta T_1 \sim 7 \times 10^{15}$ cm (where $\Delta T_1 = 1.2 \times 10^6$ sec). From the column density of the wind derived in Section 5.1 ($N_{\rm H} \sim 10^{24}$ cm$^{-2}$), we can then estimate that its density is of the order of $n_{\rm e} = N_{\rm H}/\Delta R \sim 10^8$ cm$^{-3}$.

From the photoionization modeling, we derived that the ionization of the wind is of the order of $\log(\xi/{\rm erg\,cm\,s^{-1}}) \sim 5$ (see Table 3); thus, from the definition of the ionization parameter $\xi = L_{\rm ion}/n_{\rm e}R^2$ and assuming that the ionizing luminosity[13] is $10^{45}$ erg s$^{-1}$, we derive a typical distance from the central black hole of $R \sim 10^{16}$ cm, or $\sim 700 R_{\rm g}$. Therefore, it appears that the wind is located at a distance similar to its size (or $\Delta R/R \sim 1$), which supports a scenario where during this first three observations our line of sight intercepts a rather homogeneous streamline extending from the launch radius of $64R_{\rm g}$ up to $\sim 10^3 R_{\rm g}$ and not a small clump or inhomogeneity of the wind.

We now consider the slower phase of the wind detected in OBS4, which is outflowing at $v_{\rm out} \sim -0.07\,c$. This slower zone or streamline of the wind emerges in OBS4, which occurred 16 days ($\Delta T_2 = 1.4 \times 10^6$ s) after OBS3. Since we do not know when this zone emerged, following the same arguments outlined above, we can derive an upper limit on its size scale of $\Delta R_{\rm max} < v_{\rm out,4} \times \Delta T_2 < 3 \times 10^{15}$ cm, which corresponds to $\sim 200 R_{\rm g}$. Likewise, the density is $n_{\rm e} > N_{\rm H}/\Delta R > 3 \times 10^8$ cm$^{-3}$ and $R < 6 \times 10^{15}$ cm, which is marginally lower than the location derived for the faster component of the wind. This in turn means that in OBS4 our line of sight intercepts a slower component of the wind that could be actually located closer to the black hole than the faster one. As we will discuss in Section 6.4, the possibility that in OBS4 our line of sight intercepts a slower component of the wind that could be actually located closer to the black hole than the faster one is in

[13] $L_{\rm ion}$ is the ionizing luminosity over the 1–1000 Rydberg range. Since MCG-03-58-007 is a highly obscured AGN, we cannot directly measure this luminosity; we therefore assumed, as in B18, that it is of the order of one-third of the bolometric luminosity of $3 \times 10^{45}$ erg s$^{-1}$.

agreement with a recently proposed scenario for the multiple velocity components observed in several winds. According to this model, faster components are predicted to occur at larger radii after the inner and slower wind is accelerated through UV line driving (Mizumoto et al. 2021).

### 6.3. The Extraordinary Variability of the Disk Wind

Here we discuss what we can learn on the nature of the disk wind from the variability it displayed in this monitoring. The key aspect is that MCG-03-58-007 is an extremely variable source, where both its intrinsic continuum and the wind vary on short timescales. Our spectral analysis also demonstrates that the increase in the wind opacity and thus the depth of the absorbing structures is caused by a decrease in the ionization of the wind rather than an increase in the density of the wind. Critically, this is the first case where we witnessed a dramatic variability of the wind outflowing velocity. In particular, here the magnitude of the velocity changes, which is a factor of ∼3, is much greater than those seen to date in other variable disk winds (e.g., PDS 456, Matzeu et al. 2017; IRAS 13224-3809, Chartas & Canas 2018; Parker et al. 2017; Pinto et al. 2018; APM 08279+5255, Saez & Chartas 2011). We remark that, as shown in Section 5, this variation does not depend on the model adopted to fit the broadband X-ray data.

A standard interpretation for the variation of the wind velocity would be that during OBS4 our line of sight intercepts a slower clump in the wind, which may be located farther out with respect to the faster streamline seen in the earlier observations. However, as discussed above, the rather small changes in the opacity/ionization of the wind observed between the first three observations are compatible with a relatively smooth flow. Indeed, during this monitoring we did not observe any rapid increase of the opacity of the wind, as expected from a clumpy wind. This is confirmed by our estimates of the size and location of the absorber, whose ratio ($\Delta R/R$) is of the order of unity. It is thus unlikely that in OBS4 we are observing a clump of the disk wind. An alternative possibility is that during the last observation, we observe a new slower streamline, which is launched farther out, while the faster component outflowing at $\sim -0.2\,c$ gets disrupted. Following the standard argument, where the launching radius corresponds to the escape radius ($R_{\rm min} = 2GM_{\rm BH}/v^2$), we would derive that the faster and slower components are launched from $\sim 50\,R_{\rm g}$ and $\sim 350\,R_{\rm g}$, respectively. However, this is highly implausible, as this would require that in less than 16 days the launching radius changes by an order of magnitude.

Instead, the velocity changes may be due to a response of the wind to the variability of the intrinsic emission of MCG-03-58-007. Recently, a correlation between the outflow velocity of the disk wind and the intrinsic X-ray luminosity has been reported for PDS456 (Matzeu et al. 2017), APM 08279+5255 (Saez & Chartas 2011), and IRAS 13224-3809 (Pinto et al. 2018; Chartas & Canas 2018), suggesting that these disk winds could be radiatively driven. The correlations found for these winds can be expressed as $v_{\rm out} \propto L^{\alpha}$, where the $\alpha$ ranges from ∼0.25, as measured for PDS 456 to ∼0.4 for IRAS 13224–3809. We note that for a radiatively driven wind the wind velocity is expected to be proportional to $L^{0.5}$.

In the case of MCG-03-58-007, not only are the variations more substantial than what seen in other winds, but the wind does not respond to the luminosity, whereby the wind is slower in a bright state (OBS4) and faster in the faintest state (OBS2). One could argue that for MCG-03-58-007 we are witnessing a delay in the response of the wind velocity to the luminosity, where the low velocity measured in OBS4 is caused by the low intrinsic luminosity in OBS2. However, from the above scaling relation, in order to reproduce a factor ∼2.8 velocity change, one would expect the luminosity to have changed by a factor of ∼8, while the intrinsic X-ray luminosity in OBS2 is only a factor of ∼2 lower (see Table 4 and Figure 1). The only other possibility is that there was a more substantial decrease of the luminosity in between OBS3 and OBS4; however, this is highly unlikely, as none of the previous observations caught MCG-03-58-007 in such a faint state (see Table 2 in B21).

### 6.4. The Overall Scenario of the Wind in MCG-03-58-007

We now consider the results obtained by Mizumoto et al. (2021) on the X-ray spectra predicted from the most recent hydrodynamics simulations of UV line driven disk winds, using a specific prescription for the X-ray opacity (Nomura et al. 2020). The above authors compute the evolution of the line driven wind properties (in terms of ionization, density, and velocity) as a function of the wind radius (e.g., see Figure 5 of Mizumoto et al. 2021). According to these simulations, multiple velocity components are naturally produced in the flow, once acceleration due to UV line driving is considered. In particular, they show that a highly ionized wind that is launched at a radius of about $\sim 100 R_{\rm g}$ with a velocity of $\sim 0.1\,c$ might be accompanied by a much faster component located at larger radii. Here the inner highly ionized component of the flow acts as the X-ray shielding gas, the so-called "hitchhiking gas" (Murray et al. 1995, see also Giustini & Proga 2021), which prevents the outer wind from becoming over-ionized. As the density of the wind increases with its radial distance, at about $\sim 500 R_{\rm g}$, its ionization state drops to low enough ($\log \xi < 5$) to produce the typical Fe-K absorption features. Since this gas is shielded, it can be accelerated in situ by line driving and reaches a terminal velocity of the order of $0.25\,c$. The proposed scenario can thus naturally explain the different velocity components observed in several winds, which are not necessarily different streamlines, but the evolution of a single one. Interestingly, the radii at which the acceleration occurs in the Mizumoto et al. (2021) simulations is the typical radius at which we observe the absorbing gas in MCG-03-58-007 (i.e., of about $\sim 700 R_{\rm g}$ or $\sim 10^{16}$ cm).

According to this scenario, in the first three observations we may intercept the flow after it is fully accelerated to $v_{\rm out} \sim -0.2\,c$. Conversely, during the last observation, we may be witnessing a new streamline, which is yet to be fully accelerated. The lack of the faster phase of the wind in OBS4 can be explained by simply considering the orbital timescale of the wind, which is much larger (i.e., greater than a year) than the dynamical timescale. Therefore, in the 16 days between OBS3 and OBS4, the accelerated streamline could have just simply rotated out of our line of sight.

A possible schematic for the wind in MCG-03-58-007 is shown in Figure 10. This shows a simplified geometric representation of the possible wind streamlines seen across the observations, color-coded by velocity. In the top panel, corresponding to OBS1-3, our line of sight intercepts the wind streamline, which has been accelerated up to $v_{\rm out} \sim -0.2\,c$. In the lower panel (OBS4), a new streamline has emerged in the 16 days between observations. Here, the material has not yet been fully accelerated to its maximum terminal velocity, and a

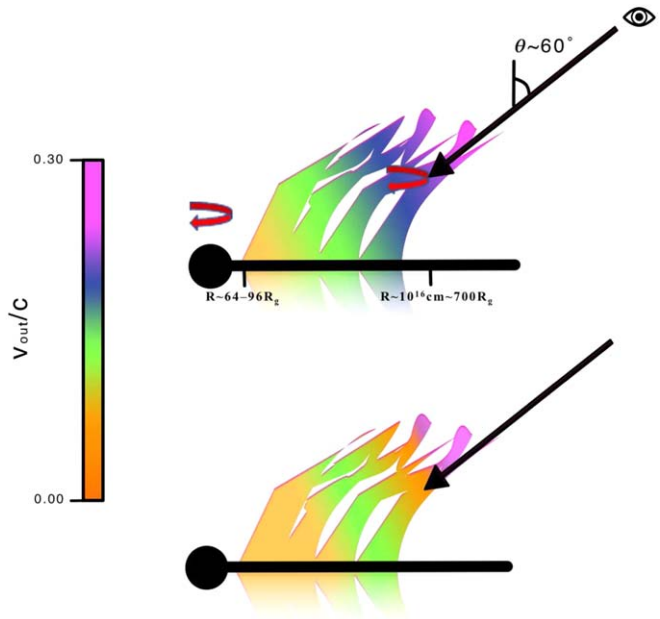


**Figure 10.** A simple schematic of the wind streamlines, color-coded according to velocity—from slow to fast—orange, green, blue, and violet (following the colors adopted by Mizumoto et al. 2021). The upper panel is representative of the first three observations, where our line of sight intercepts a fast wind component ($v_{\rm out} \sim -0.2\ c$), close to the likely terminal velocity. The red arrows represent the wind and black hole axis rotation. In the two weeks between observations 3 and 4, a new wind streamline emerges, and the previous streamline has rotated out of the line of sight. A slower ($v_{\rm out} \sim -0.07\ c$) velocity component is intercepted (lower panel), which is yet to be accelerated to its terminal velocity. Approximate size scales for the launch radius and the wind streamlines are marked on the figure. Note that the distances are not to scale.

lower velocity ($v_{\rm out} \sim -0.07\ c$) has been observed. Future, more intensive observations may be able to track further such velocity changes and how they occur, with a fine time sampling.

Looking back at the previous observations, these two phases were simultaneously in our line of sight in the Suzaku and possibly in the Swift observations (see B18 and B21). In particular, two deep absorption features were present in the Suzaku spectra at ∼7.4 keV and ∼8.5 keV (see B18). These structures could be accounted for by two highly ionized and high column density outflowing absorbers with $v_{\rm out1}/c \sim -0.07$ and $v_{\rm out2}/c \sim -0.2$, matching the two velocities measured for the wind in this new monitoring campaign. Interestingly, in the past (during the long look with XMM-Newton and NuSTAR performed in 2015), we also witnessed an occultation event, where the opacity of the disk wind rapidly increased due to a possible clump with a higher than usual density (and consequently lower ionization). From the duration of the occultation event, we derived a location for this higher-density and lower ionization clump of the wind of the order of $R \sim 5 \times 10^{15}$ cm, which is consistent with the location of the wind derived in this work. An intriguing possibility is that these higher density clumps are indeed the site of acceleration of the wind due to line driving. We note that recent works (Dannen et al. 2020; Waters et al. 2021) show that AGN winds naturally become clumpy; although these works focus on thermally driven winds, a similar process may be at work in all winds. As winds evolve and propagate, the initial small inhomogeneities of the density or temperature of the gas will form individual denser/colder clumps or clouds, which can then be the site of additional acceleration.

## 7. Summary and Conclusion

We presented the results of a series of simultaneous XMM-Newton and NuSTAR observations of MCG-03-58-007 performed in May–June 2019. During this campaign, both the intrinsic emission and the disk wind of MCG-03-58-007 varied on timescales as short as 4 days. We confirm that the disk wind in MCG-03-58-007 is persistent, as it is detected in all the observations, but highly variable in both the opacity and velocity. Indeed, both the XSTAR and the DISKWIND models show that the variability of the disk-wind opacity can be explained by changes in the ionization of the wind, which becomes less transparent during the second observation. We also confirm that, regardless of the model adopted, the kinetic power of the disk wind is well above the kinetic energy carried by the molecular gas phase.

The novel and most striking result, obtained with this new observational campaign, is that the outflowing velocity changed by a factor of ∼3 in just 16 days, dropping from $v/c \sim -0.2$ to $v/c \sim -0.074$. To our knowledge, this is the first case where such a dramatic variability of the wind velocity is observed. The size scale and location of the absorber, derived from variability arguments, suggest that we are observing a rather homogeneous flow that is located at $\sim 700 R_{\rm g}$ (or $\sim 10^{16}$ cm) and not different small clumps of the wind. The rapid variation in the wind velocity is also incompatible with a scenario whereby we intercept streamlines of the disk wind launched at different radii. Indeed, this would imply that the launching radius changes from a few tens to a few hundreds of $R_{\rm g}$ in just a couple of weeks, which is implausible. A more likely scenario is that we observe the same streamline of the wind, but the different velocity components are simply due to the acceleration of the wind, as recently proposed by Mizumoto et al. (2021). According to this scenario, in the first three observations, we intercept the flow after it is accelerated to $v_{\rm out} \sim -0.2\ c$. Conversely, during the last observation, we see only the slower pre-accelerated streamline, while the accelerated phase could have simply rotated out of our line of sight.

Our results on the disk wind of MCG-03-58-007 emphasize the importance of monitoring programs of disk winds. A single snapshot can give an incomplete picture of them, and only observations at different timescales of the winds can fully reveal their complex structure. Further monitoring programs of MCG-03-58-007 and similarly variable winds are now clearly required to better understand their structure and to shed light on their driving mechanisms. These, combined with ongoing efforts with the disk-wind simulations, will allow us to better understand the evolution of the AGN winds and properly quantify the energy feedback exerted on the galactic environment.

We thank the referee for the useful comments, which improved this paper. We would like to thank Stuart Sim for the use of his disk-wind radiative transfer code and for providing input into the generation of the disk-wind synthetic spectra used in this paper. This research has made use of data obtained from XMM-Newton, an ESA science mission with instruments and contributions directly funded by ESA Member States and the USA (NASA), and from the NuSTAR mission, a project led by the California Institute of Technology, managed by the Jet Propulsion Laboratory, and funded by NASA. This research has made use

of the NuSTAR Data Analysis Software (NuSTARDAS) jointly developed by the ASI Science Data Center and the California Institute of Technology. V.B. acknowledges financial support through the NASA grant 80NSSC20K0793. V.B., R.D.C., and P. S. acknowledge financial contribution from the agreements ASI-INAF n.2017-14-H.0. M.G. is supported by the "Programa de Atracción de Talento" of the Comunidad de Madrid, grant N0. 2018-T1/TIC-11733.

*Software:* xstar Kallman et al. 2004), diskwind code (Sim et al. 2008, 2010a, 2010b), SAS (v16.0.0; Gabriel et al. 2004), FTOOLS (v6.27.2; Blackburn 1995), XSPEC (v12.11; Arnaud 1996).

## ORCID iDs

V. Braito https://orcid.org/0000-0002-2629-4989
J. N. Reeves https://orcid.org/0000-0003-3221-6765
P. Severgnini https://orcid.org/0000-0001-5619-5896
L. Ballo https://orcid.org/0000-0002-5036-3497
C. Cicone https://orcid.org/0000-0003-0522-6941
R. Della Ceca https://orcid.org/0000-0001-7551-2252
M. Giustini https://orcid.org/0000-0002-1329-658X

## References

Arnaud, K. A. 1996, in ASP Conf. Ser., 101, Astronomical Data Analysis Software and Systems V, ed. G. H. Jacoby & J. Barnes (San Francisco, CA: ASP), 17
Bischetti, M., Piconcelli, E., Feruglio, C., et al. 2019, A&A, 628, A118
Blackburn, J. K. 1995, in ASP Conf. Ser., 77, Astronomical Data Analysis Software and Systems IV, ed. R. A. Shaw, H. E. Payne, & J. J. E. Hayes (San Francisco, CA: ASP), 367
Braito, V., Reeves, J. N., Matzeu, G. A., et al. 2018, MNRAS, 479, 3592
Braito, V., Reeves, J. N., Severgnini, P., et al. 2021, MNRAS, 500, 291
Chartas, G., Brandt, W. N., Gallagher, S. C., & Garmire, G. P. 2002, ApJ, 579, 169
Chartas, G., & Canas, M. H. 2018, ApJ, 867, 103
Cicone, C., Maiolino, R., Gallerani, S., et al. 2015, A&A, 574, A14
Cicone, C., Maiolino, R., Sturm, E., et al. 2014, A&A, 562, A21
Dannen, R. C., Proga, D., Waters, T., & Dyda, S. 2020, ApJL, 893, L34
Di Matteo, T., Springel, V., & Hernquist, L. 2005, Natur, 433, 604
Edelson, R., Turner, T. J., Pounds, K., et al. 2002, ApJ, 568, 610
Faucher-Giguère, C.-A., & Quataert, E. 2012, MNRAS, 425, 605
Ferrarese, L., & Merritt, D. 2000, ApJL, 539, L9
Feruglio, C., Fiore, F., Carniani, S., et al. 2015, A&A, 583, A99
Fiore, F., Feruglio, C., Shankar, F., et al. 2017, A&A, 601, A143
Fluetsch, A., Maiolino, R., Carniani, S., et al. 2019, MNRAS, 483, 4586
Fukumura, K., Kazanas, D., Contopoulos, I., & Behar, E. 2010, ApJ, 715, 636
Fukumura, K., Kazanas, D., Shrader, C., et al. 2017, NatAs, 1, 0062
Fukumura, K., Tombesi, F., Kazanas, D., et al. 2015, ApJ, 805, 17
Gabriel, C., Denby, M., Fyfe, D. J., et al. 2004, in ASP Conf. Ser., 314, Astronomical Data Analysis Software and Systems (ADASS) XIII, ed. F. Ochsenbein, M. G. Allen, & D. Egret (San Francisco, CA: ASP), 759
Gebhardt, K., Bender, R., Bower, G., et al. 2000, ApJL, 539, L13
Giustini, M., & Proga, D. 2012, ApJ, 758, 70
Giustini, M., & Proga, D. 2021, IAUS, 356, 82
Gofford, J., Reeves, J. N., McLaughlin, D. E., et al. 2015, MNRAS, 451, 4169
Gofford, J., Reeves, J. N., Tombesi, F., et al. 2013, MNRAS, 430, 60
Hagino, K., Odaka, H., Done, C., et al. 2015, MNRAS, 446, 663
Hagino, K., Odaka, H., Done, C., et al. 2016, MNRAS, 461, 3954
Harrison, F. A., Craig, W. W., Christensen, F. E., et al. 2013, ApJ, 770, 103
HI4PI Collaboration, Ben Bekhti, N., Flöer, L., et al. 2016, A&A, 594, A116
Hopkins, P. F., & Elvis, M. 2010, MNRAS, 401, 7
Kallman, T. R., Palmeri, P., Bautista, M. A., Mendoza, C., & Krolik, J. H. 2004, ApJS, 155, 675
Kato, Y., Mineshige, S., & Shibata, K. 2004, ApJ, 605, 307
Kazanas, D., Fukumura, K., Behar, E., Contopoulos, I., & Shrader, C. 2012, AstRv, 7, 92
King, A. 2003, ApJL, 596, L27
King, A. 2005, ApJL, 635, L121
King, A., & Pounds, K. 2015, ARA&A, 53, 115
King, A. R. 2010, MNRAS, 402, 1516
Krongold, Y., Nicastro, F., Elvis, M., et al. 2007, ApJ, 659, 1022
Luminari, A., Piconcelli, E., Tombesi, F., et al. 2018, A&A, 619, A149
Lutz, D., Sturm, E., Janssen, A., et al. 2020, A&A, 633, A134
Magorrian, J., Tremaine, S., Richstone, D., et al. 1998, AJ, 115, 2285
Matzeu, G. A., Braito, V., Reeves, J. N., et al. 2019, MNRAS, 483, 2836
Matzeu, G. A., Reeves, J. N., Braito, V., et al. 2017, MNRAS, 472, L15
Matzeu, G. A., Reeves, J. N., Nardini, E., et al. 2016, MNRAS, 458, 1311
Mewe, R., Gronenschild, E. H. B. M., & van den Oord, G. H. J. 1985, A&AS, 62, 197
Mitsuda, K., Bautz, M., Inoue, H., et al. 2007, PASJ, 59, S1
Mizumoto, M., Izumi, T., & Kohno, K. 2019, ApJ, 871, 156
Mizumoto, M., Nomura, M., Done, C., Ohsuga, K., & Odaka, H. 2021, MNRAS, 503, 1442
Murray, N., Chiang, J., Grossman, S. A., & Voit, G. M. 1995, ApJ, 451, 498
Nardini, E., & Zubovas, K. 2018, MNRAS, 478, 2274
Nomura, M., & Ohsuga, K. 2017, MNRAS, 465, 2873
Nomura, M., Ohsuga, K., & Done, C. 2020, MNRAS, 494, 3616
Parker, M. L., Matzeu, G. A., Guainazzi, M., et al. 2018, MNRAS, 480, 2365
Parker, M. L., Pinto, C., Fabian, A. C., et al. 2017, Natur, 543, 83
Pinto, C., Alston, W., Parker, M. L., et al. 2018, MNRAS, 476, 1021
Pounds, K. A., Reeves, J. N., King, A. R., et al. 2003, MNRAS, 345, 705
Proga, D., & Kallman, T. R. 2004, ApJ, 616, 688
Proga, D., Stone, J. M., & Kallman, T. R. 2000, ApJ, 543, 686
Reeves, J. N., & Braito, V. 2019, ApJ, 884, 80
Reeves, J. N., Braito, V., Gofford, J., et al. 2014, ApJ, 780, 45
Reeves, J. N., Braito, V., Nardini, E., et al. 2018a, ApJ, 867, 38
Reeves, J. N., Lobban, A., & Pounds, K. A. 2018b, ApJ, 854, 28
Reeves, J. N., O'Brien, P. T., & Ward, M. J. 2003, ApJL, 593, L65
Saez, C., & Chartas, G. 2011, ApJ, 737, 91
Sim, S. A., Long, K. S., Miller, L., & Turner, T. J. 2008, MNRAS, 388, 611
Sim, S. A., Miller, L., Long, K. S., Turner, T. J., & Reeves, J. N. 2010a, MNRAS, 404, 1369
Sim, S. A., Proga, D., Miller, L., Long, K. S., & Turner, T. J. 2010b, MNRAS, 408, 1396
Sirressi, M., Cicone, C., Severgnini, P., et al. 2019, MNRAS, 489, 1927
Tatum, M. M., Turner, T. J., Sim, S. A., et al. 2012, ApJ, 752, 94
Tombesi, F., Cappi, M., Reeves, J. N., & Braito, V. 2012, MNRAS, 422, L1
Tombesi, F., Cappi, M., Reeves, J. N., et al. 2010, A&A, 521, A57
Tombesi, F., Meléndez, M., Veilleux, S., et al. 2015, Natur, 519, 436
Tombesi, F., Veilleux, S., Meléndez, M., et al. 2017, ApJ, 850, 151
Vaughan, S., Edelson, R., Warwick, R. S., & Uttley, P. 2003, MNRAS, 345, 1271
Veilleux, S., Maiolino, R., Bolatto, A. D., & Aalto, S. 2020, A&ARv, 28, 2
Waters, T., Proga, D., & Dannen, R. 2021, ApJ, 914, 62
Wilms, J., Allen, A., & McCray, R. 2000, ApJ, 542, 914
Zubovas, K., & King, A. 2012, ApJL, 745, L34
Zubovas, K., & King, A. 2016, MNRAS, 462, 4055
Zubovas, K., & Nardini, E. 2020, MNRAS, 498, 3633